

Recent Advances in Fabrication Techniques of Perovskite Solar Cells: A Review

Alborz Ehtesham, WeiWen Wong, H.Y. Wong and Mukter Zaman

Faculty of Engineering (FOE), Multimedia University, 63100 Cyberjaya, Malaysia

Article history

Received: 28-08-2016

Revised: 25-10-2016

Accepted: 25-11-2016

Corresponding Author:

Mukter Zaman

Faculty of Engineering (FOE),

Multimedia University, 63100

Cyberjaya, Malaysia

Tell: +6010-5391581

Email: mukter@mmu.edu.my

Abstract: In this study, thorough review is performed on various reported fabrication techniques of the Perovskite Solar Cell (PSC) and the Hole Transport Materials (HTM) layer, in order to provide a critical insight on the direction for further advancement in related fields as well as a better understanding on the device physics. So far, the best short-circuit current density of 22.9 mA/cm² has been reported in CH₃NH₃PbI_{3-x}Cl_x scaffold by TiCl₄ nanorods treated by NRS and the best open circuit voltage of 0.763V has been reported in TiO₂/perovskite/spiro-OMeTAD/Au. On the other hand, so far the highest PCE of the PSCs reported in the literature is 19.3%. Interestingly, PSC with 200nm mesoporous TiO₂ has been reported to achieve PCE value of 16.46%. A 5-layer TiO₂/perovskite/spiro-OMeTAD/Au integrated with 40 nm ZnO thin film has been reported to achieve Fill Factor (FF) of 76%. Although promising data has been obtained through numerous researches, there are still many other optimizations yet to be done before mass commercialization of PSC is possible. Optimizing the fabrication process of carrier transport material as well as the incorporation of sensitizer into the device structure are the key aspects that should be focused on in future researches.

Keyword: Perovskite, Solar Cell, Fabrication, Efficiency, Influence Effect, Replicable Energies

Introduction

Benchmarking of PSC Research and Development

Perovskite is a special type of solar cell material, named after the Russian mineralogist, L. A. Perovski (1792-1856) and is often considered as one of the most promising types of next-generation solar cell material. PSC has the perovskite crystal structure, which is shown in Fig. 1a and generally consists of organic and inorganic materials. The organic material converts solar energy to electrical energy, while the inorganic material provides the crystal structure. Generally, the PSC device is fabricated on top of a conductive substrate. The device structure consists of a layer of Electron Transport Material (ETM), followed by a perovskite sensitizer which converts photons into electrons and holes, a layer of Hole Transport Material (HTM) and finally the electrode layers to complete the circuit externally with the conductive substrate. A typical device structure of a PSC is shown in Fig. 1b. Despite the considerable amount of speculations that arose when PSC was first introduced in 2009, PSC is now considered to have a promising future because of its

high energy conversion efficiency at lower cost than conventional solar cells, as well as its high versatility which allows it to be coated on various types of substrate materials. Although the commercialization progress of PSC is still currently in its infancy stage, its fabrication methods are found to be amazingly versatile, as there are many proven alternatives to fabricate PSC successfully.

In terms of energy conversion efficiency, PSC has been improving dramatically in the last few years. Researchers have demonstrated that the energy conversion efficiency of PSCs could go up to 20%. Nevertheless, stability of PSC remains as a critical concern. While conventional silicon-based solar cells can last for up to a quarter century without significant degradation in its performance, PSC with the best performance reported so far is only capable to maintain optimal performance for up to 100 h (Alharbi *et al.*, 2014; Peplow, 2014). The relatively poor stability of PSC is because perovskite compound, which is water soluble, would break down easily in the presence of sunlight. Therefore, the current challenge in the development of PSCs is the stability issue rather than performance issue.

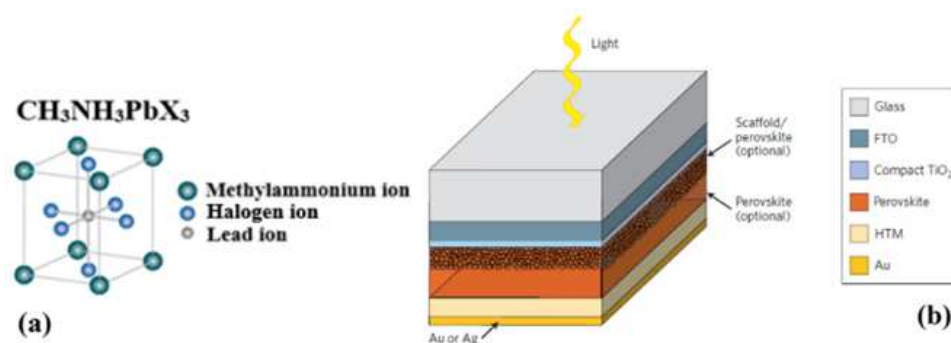


Fig. 1. (a) The crystal structure of perovskite (b) the structure of perovskite-based solar cell (Green *et al.*, 2014)

In this review, the fundamental working principle of PSC will be discussed along with all the reported possible combinations of PSC components, followed by different fabrication techniques of the PSC and HTM layers, as well as the synthesis processes of the PSC components reported in the literature. A critical review on different reported conditions such as but not limited to various atmosphere condition, thin film properties, HTM, electron transport, external electric field, blocking layer, transport layer, CBO and VBO absorber layer, heat treated ion assisted film, thermal annealed effect, reduced graphene oxide, blade coating and low temperature solution will be provided systematically. This review would be useful to benchmark all the research activities for PSC in order to obtain an insight for future studies on related fields.

Overview of Synthesis Methods of PSC

Different types of perovskite can be fabricated in different methods, among which fabrication methods of $\text{CH}_3\text{NH}_3\text{PbI}_3$ (iodine based), $\text{CH}_3\text{NH}_3\text{Sn}_{0.5}\text{Pb}_{0.5}\text{I}_3$, $\text{CH}_3\text{NH}_3\text{SnI}_3$, $\text{CH}_3\text{NH}_3\text{PbBr}_3$ (bromine based), $\text{K}_2\text{La}_2\text{Ti}_3\text{O}_{10}$, $\text{La}_{0.7}\text{Sr}_{0.3}\text{MnO}_3$, hybrid PSC with a planar heterojunction structure have been reported as the most promising methods and will therefore be explained in this section. This section will end with a summary of the different fabrication methods discussed.

Synthesis of $\text{CH}_3\text{NH}_3\text{PbI}_3$ Sensitizer (Iodine-based)

The most well-known perovskite compound is $\text{CH}_3\text{NH}_3\text{PbI}_3$, which can be fabricated by mixing PbI_2 and $\text{CH}_3\text{NH}_3\text{I}$. In order to produce the $\text{CH}_3\text{NH}_3\text{I}$ compound, methylamine (30%) is mixed with HI (45%) in ice-bath for few hours so that the chemicals can react effectively (Jeon *et al.*, 2014). The solution also can be synthesized under nitrogen atmosphere at 0°C (Wang *et al.*, 2015). After that, the evaporation of the methylamine and HI solvent will be conducted at high temperature. The remaining solid is dissolved in ethanol and recrystallized in diethyl ether. From this process, $\text{CH}_3\text{NH}_3\text{I}$ compound which is pure-white in

color (Xin *et al.*, 2014; Sheikh *et al.*, 2015) would be obtained. It can also be synthesized by adding 24 mL of methylamine and 10 mL of hydroiodic acid with 100 mL of ethanol with continuous stirring for 2 h in ice bath. With a help of rotary evaporator at 50°C to exclude the solvent, the precipitate is collected. Later on the product is recrystallized in ethanol and followed by the filtering and washing the end product with diethyl ether. Next step is drying for 24 h at 60°C in vacuum oven (Dkhissi *et al.*, 2015; Li *et al.*, 2015).

$\text{CH}_3\text{NH}_3\text{PbI}_3$ can be fabricated by dissolving $\text{CH}_3\text{NH}_3\text{I}$ and PbI_2 in gamma-butyrolactone and maintaining uniform stirring for 24 h. Next, the solution is deposited on top of the substrate by spin coating and heated up for 30 min at 100°C . Another method to synthesize $\text{CH}_3\text{NH}_3\text{PbI}_3$ is by dissolving PbI_2 in N, N-dimethylformamide at 70°C (Zhang *et al.*, 2015) and then spin coating it on top of the substrate. The layer is then dried by heating the substrate at 70°C for 15 min. Then, the substrate is dipped into 2-propanol solution that contains $\text{CH}_3\text{NH}_3\text{I}$ to form $\text{CH}_3\text{NH}_3\text{PbI}_3$ layer (Della Gaspera *et al.*, 2015). Another method to fabricate perovskite $\text{CH}_3\text{NH}_3\text{PbI}_3$ is by adding 30 mL of hydrochloric acid with methylamine and stirring the solution without any interruption for 2 h. Then, the precipitates of $\text{CH}_3\text{NH}_3\text{I}$ are collected by distillation at 50°C under reduced pressure and washed with diethyl ether. Next, the precipitates are recrystallized using ethanol and diethyl ether and dried in a vacuum oven at 70°C for 24 h. The purified $\text{CH}_3\text{NH}_3\text{I}$ powder is dissolved in gamma-butyrolactone with PbI_2 overnight at 60°C with continuous stirring to form the precursor (Xiao *et al.*, 2014). In addition to the perovskite structure, another compound, known as $\text{CH}_3\text{NH}_3\text{PbI}_3 \cdot x\text{Cl}_x$, has been reported in similar context. It can be fabricated with Methylamine Iodide (MAI) to PbCl_2 molar ratio of 3:1, where the mixed solution is stirred for 24 h at 60°C and then added into the prepared $\text{CH}_3\text{NH}_3\text{PbI}_3$ (Wang *et al.*, 2015; Sheikh *et al.*, 2015).

Several performance curves of the $\text{CH}_3\text{NH}_3\text{PbI}_3$ PSC with varying film thicknesses, when illuminated from the

FTO side, are shown in Fig. 2. From the I-V curve $\text{CH}_3\text{NH}_3\text{PbI}_3$ PSC with 290 nm film thickness is reported to have the highest current density compared to PSC with other film thicknesses. At the same time, the 290 nm PSC also showed highest IPCE and lowest transmittance at wavelength ranging from 550 to 800 nm (Della Gaspera *et al.*, 2015).

Synthesis of Cocktail PSC

The substrate material used to fabricate cocktail perovskite is FTO glass/compact. First, the patterning and cleaning of the substrate is carried out. Then, by using spray pyrolysis method titanium(IV) cetylacetonate is coated on top of the substrate at 470°C , followed by dipping the substrate in TiCl_4 aqueous solution at 70°C for 30 min, before heating the substrate in air at 500°C . The deposition of TiO_2 nanoparticles on the substrate can be done by

spin coating method, followed by 30 min of heating in air at 500°C . The next step is conducted under N_2 atmosphere to prepare the perovskite layer. Mixture of $\text{SnI}_2/\text{PbI}_2$ and $\text{CH}_3\text{NH}_3\text{I}$ (40 wt%, 1:1/mol) in DMF is spin coated and heated at 60°C for 30 min on a porous titania layer. Polymers are dissipated by spin coating on the substrate to employ the hole transporting layer P3HT. The flow diagram of the whole experiment procedure is shown in Fig. 3a (Ogomi *et al.*, 2014; Bradley, 2015). Figure 3b shows the stability of this perovskite in the air with and without PbI_2 . Without PbI_2 , a rapid decrement in the 900 nm absorption in air can be observed. Eventually, the absorption drops from 1.0 to 0 in 60 min. Meanwhile, when PbI_2 is incorporated in the compound, the 900 nm absorption is relatively stable in air. The efficiency of this PSC is reported to be 14.4% (Ogomi *et al.*, 2014).

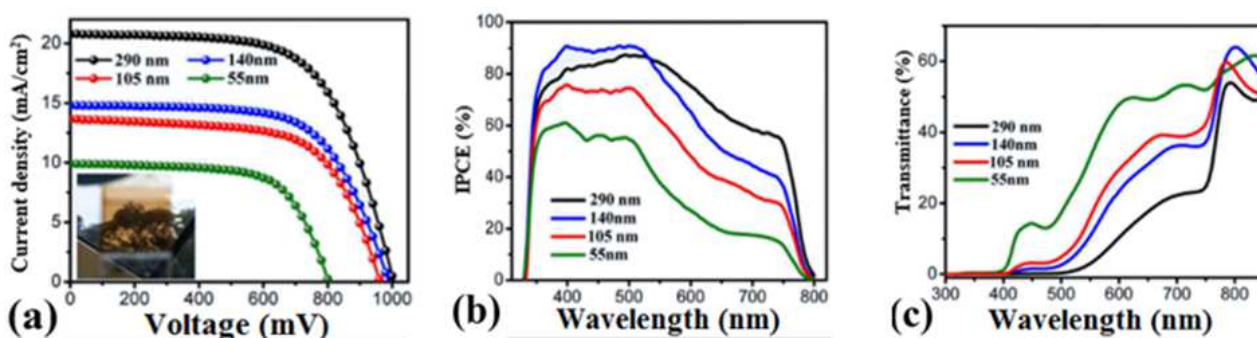


Fig. 2. (a) Current over voltage curves of PSC, with inset showing a photograph of a semitransparent PSC (b) IPCE and (c) transmittance spectra of complete PSCs with different $\text{CH}_3\text{NH}_3\text{PbI}_3$ film thicknesses (Della Gaspera *et al.*, 2015)

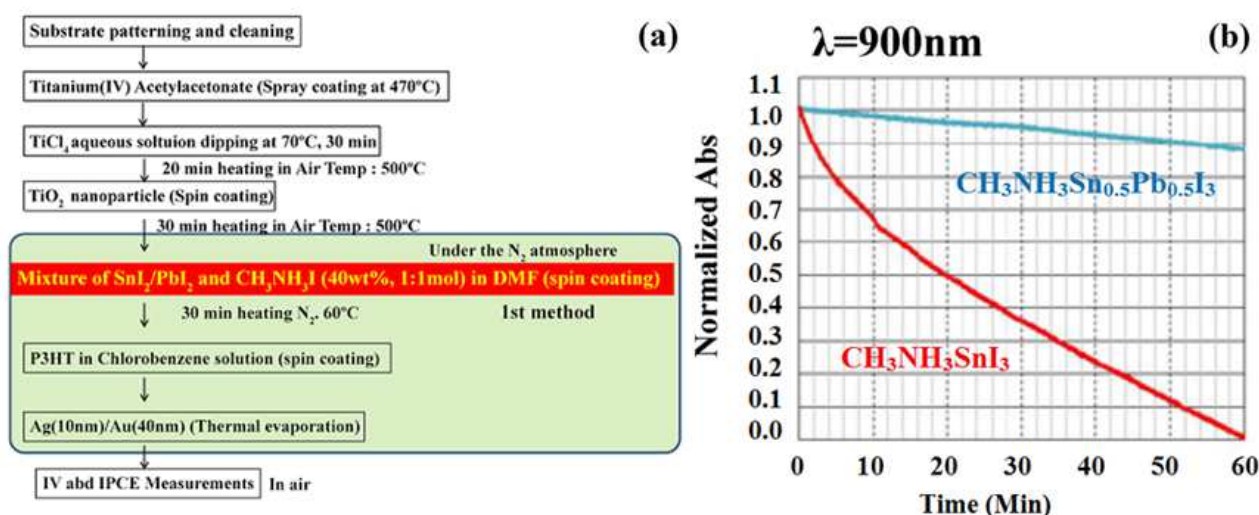


Fig. 3. (a) Preparation procedures of PSC under nitrogen gas condition (Ogomi *et al.*, 2014) (b): Stability of PSC in air (Ogomi *et al.*, 2014)

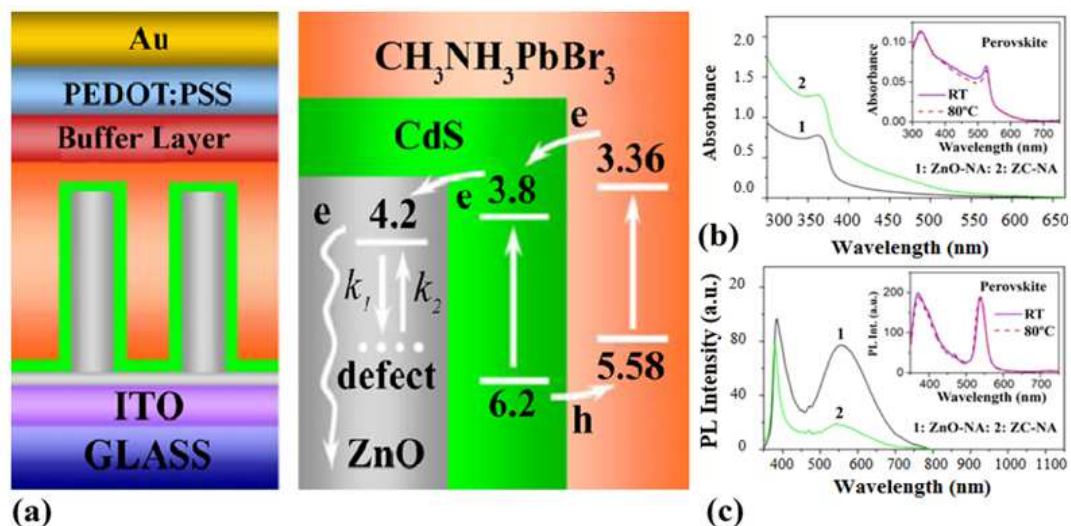


Fig. 4. (a): Structure of the device architecture (b): Absorption spectra (c): Room temperature PL (excited at 325 nm) spectra of ZnO-NA and ZC-NA samples (Liu *et al.*, 2015)

Synthesis of $\text{CH}_3\text{NH}_3\text{PbBr}_3$ (Bromine-based)

The synthesis of $\text{CH}_3\text{NH}_3\text{PbBr}_3$ starts by mixing 48 mL of methylamine with 57 mL of hydrobromic acid for 2 h with constant stirring. After that, by evaporating the solution for 1 h at 50°C , the precipitate can be recovered. The arrows in Fig. 4a indicates the transfer of charge carriers, namely electrons and holes, inside the compound structure. The inset images in Fig. 4b and 4c are showing the absorption and room temperature photoluminescence (excited at 325 nm) spectra of the $\text{CH}_3\text{NH}_3\text{PbBr}_3$ films with and without thermal annealing at 80°C . The product of the chemical mixing is recrystallized by dipping into tetrahydrofuran twice and followed by drying process in vacuum oven at 60°C overnight. The dried $\text{CH}_3\text{NH}_3\text{Br}$ is then mixed with PbBr_2 in N, N-dimethylformamide with constant stirring for 12 h at 60°C to form the perovskite precursor (Liu *et al.*, 2015).

Synthesis of $\text{K}_2\text{La}_2\text{Ti}_3\text{O}_{10}$ Sensitizer

PSC can be fabricated from other compound such as $\text{K}_2\text{La}_2\text{Ti}_3\text{O}_{10}$. It is prepared by conventional solid state reactions. First, stoichiometric amounts of K_2CO_3 , La_2O_3 and TiO_2 powders are mixed. In order to compensate the volatilization of the mixture, there is an excess amount of carbonate added. The mixture is calcinated in platinum crucible at 1000°C in air for 24 h. In order to remove the excess alkali in the substance, the product is washed by distilled water and dried at 500°C to obtain anhydrous oxides. Next step is to protonate the surface. The powder form product is immersed in aqueous HNO_3 solution at room temperature for 15 h. Then, centrifuging process is carried out to obtain white precipitates. Later, the precipitate is immersed in aqueous ammonia solution for 15 h in nitrogen

environment. Lastly, the precipitated powder is dried and annealed with the presence of nitrogen gas for 1 h at 400°C . The end product is a light-yellowish powder. The absorbance and transmittance spectra of this type of PSC are shown in Fig. 5a and 5b (Huang *et al.*, 2010).

Synthesis of $\text{La}_{0.7}\text{Sr}_{0.3}\text{MnO}_3$ Nano-Perovskite

$\text{La}_{0.7}\text{Sr}_{0.3}\text{MnO}_3$ is prepared using the citrate method. The chemicals used in the synthesis process are 0.0031 mol of $\text{La}(\text{NO}_3)_3 \cdot 6\text{H}_2\text{O}$, 0.0043 mol of $\text{Mn}(\text{NO}_3)_2 \cdot 4\text{H}_2\text{O}$ and 0.0013 mol of $\text{Sr}(\text{NO}_3)_2$ precursors in the presence of 0.0205 mol of citric acid. All the chemicals with respective number of moles are added together and left to evaporate overnight at 60°C . Then, the products are dried subsequently at 80°C and 150°C for 24 h. To get the end product, the mixture is calcinated for 9 h at 900°C . The resulting material is powdered. The absorbance of this type of PSC can be seen in Fig. 5c (Ghiasi and Malekzadeh, 2014).

Synthesis of Hybrid PSC with Planar Heterojunction Structure (ITO/ZnO/ $\text{CH}_3\text{NH}_3\text{PbI}_3$ /spiro-OMeTAD/Ag)

An organic/inorganic hybrid solar cell is the combination of a mesoporous scaffold, an organic hole transporter and a perovskite light absorber. They have emerged at the forefront of solution process to enable the operation of photovoltaic devices. The sintering process for mesoporous metal-oxide support requires temperature up to 500°C for 8 h. The hybrid PSC device architecture, photograph of a bending test on the hybrid PSC fabricated on a flexible PET substrate, J-V characteristic curve, IPCE spectrum and the efficiency curve of the hybrid PSC are shown in Fig. 6a-f.

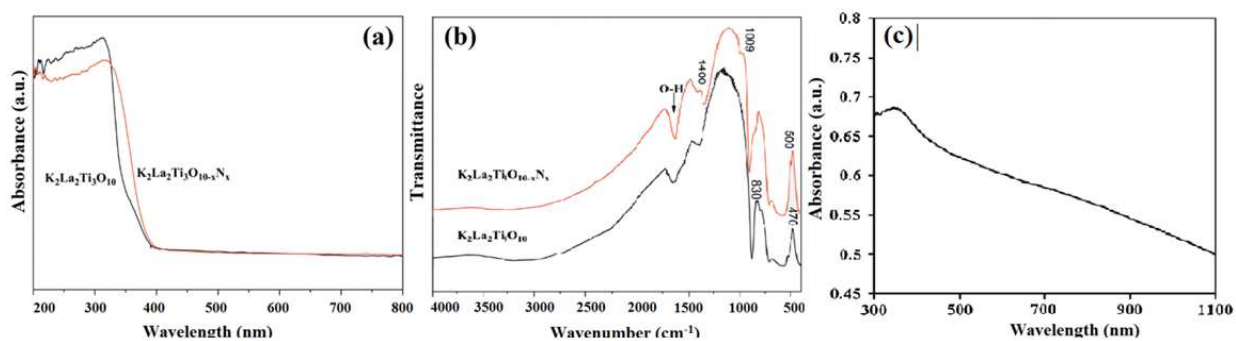


Fig. 5. (a) Absorbance spectra and (b): Transmittance spectra of $K_2La_2Ti_3O_{10}$ powder and nitrogen-doped $K_2La_2Ti_3O_{10-x}N_x$ powder (Huang *et al.*, 2010) (c): UV-Vis absorbance spectrum of $La_{0.7}Sr_{0.3}MnO_3$ sample (Ghiasi and Malekzadeh, 2014)

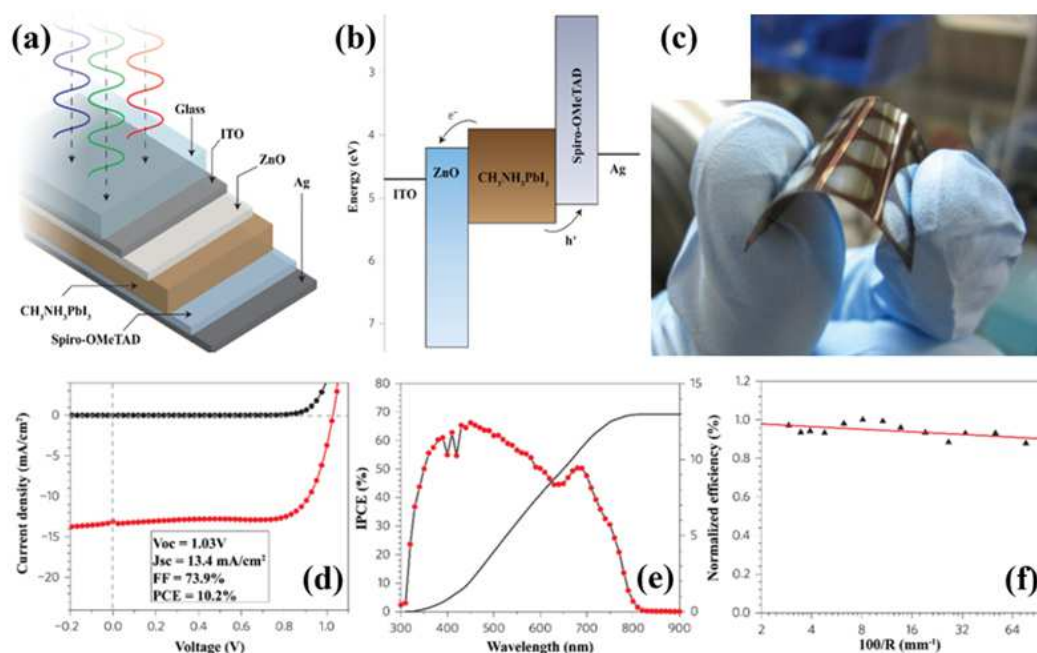


Fig. 6. (a) Device architecture of the ITO/ZnO/ $CH_3NH_3PbI_3$ /spiro-OMeTAD/Ag cells (b) Energy levels (relative to vacuum) of the various device components (c) Photograph of device (d) J-V characteristic curve (e) IPCE spectrum (f) Normalized PCE (measured on a flat device) after first bending the substrate around a cylindrical object of the specified radius (R) (Liu and Kelly, 2014)

Thin film of ZnO nanoparticles can be used as an electron transport layer in $CH_3NH_3PbI_3$ based solar cells. ZnO layer does not require sintering and it is thinner than TiO_2 . Based on these advantages a flexible solar cell with power efficiency of 10% can be fabricated. By using ZnO thin film, the performance of the solar cells prepared on rigid substrates is improved also. These cells can achieve a power conversion efficiencies as high as 15.7% under measurement of AM1.5 G illumination. First step is the synthesis of ZnO nanoparticles. ZnO nanoparticles are prepared using a precipitation method with zinc acetate as precursor material and KOH as precipitating agent. The ZnO nanoparticles solution is filtered by going through a 0.45 mm PVDF syringe filter. This solar is fabricated on ITO coated glass

substrate that has the $20\Omega sq^{-1}$ sheet resistance. Then, a thin layer of ZnO nanoparticle is spin coated on the substrate at 3,000 RPM for 30 sec. Following that, a solution of PbI_2 (dissolved in N, N-dimethylformamide with concentration of $460 mg mL^{-1}$) is spin coated on the top of the ZnO layer at 3,000 RPM for 15 sec. After several minutes of drying in the air, the substrate is dipped into $10 mg mL^{-1}$ solution of CH_3NH_3I for 40 sec before being dried under a flow of clean air. The spiro-OMeTAD base hole transfer layer (80 mg spiro-OMeTAD, 28.5 mL 4-tertbutylpyridine and 17.5 mL lithium-bis(trifluoromethanesulfonyl)imide (Li-TFSI) solution (520 mg Li-TFSI in 1 mL acetonitrile) all dissolved in 1 mL chlorobenzene) is deposited by 4,000 RPM for 30 sec. Finally, at base pressure of 2×10^{-6}

mbar, a 150 nm-thick silver layer is deposited by thermal evaporation. All the fabrication steps are carried out under ambient conditions.

The photovoltaic parameter graphs of this type of PSC are shown in Fig. 6. Figure 6d shows the J-V characteristic curve measurements of the highest-performing ITO/ZnO/CH₃NH₃PbI₃/spiro-OMeTAD/Ag flexible device under 100 mWcm⁻² AM1.5G illumination and in the dark. Figure 6e represents the IPCE spectrum of the highest-performing ITO/ZnO/CH₃NH₃PbI₃/spiro-OMeTAD/Ag flexible device. The integrated product of the IPCE spectrum with the AM1.5G photon flux is also shown (black line). All measurements in Fig. 6d-f were performed on a single device and were performed from the highest radius of curvature to the lowest (Liu and Kelly, 2014).

Synthesis of Inorganic-Organic Hybrid PSC

The fabrication methodology for a bilayer architecture has the key features of full solution-based processes to synthesize mesoscopic and planar structures. In the fabrication process, poly(triarylamine) acts as the HTM layer and CH₃NH₃Pb(I_{1-x}Br_x), x = 0.1-0.15 acts as the absorber layer. First, with the spray pyrolysis method a thick layer of TiO₂ (70 nm) is deposited on top of a F-doped SnO₂ (FTO, Pilkington, TEC8) substrate. In order to avoid direct contact between hole conducting layer and the FTO, a 20 mM titanium diisopropoxide bis(acetylacetonate) solution is used at 450°C. Next, a 200-300 nm thick mesoporous TiO₂ film is spin coated on top of the bl-TiO₂/FTO substrate. Then, in order for the organic components to be removed, the film is calcinated at 500°C for 1 h in air. After that, 27.86 mL of CH₃NH₂ (40% in

methanol) and 30 mL of HI (57 wt% in water) or 44 mL HBr (48 wt% in water) are mixed in a 250 mL round-bottom flask at 0°C for 4 h with continuous stirring. By evaporation at 55°C for 1 hour, the precipitate is recovered. MAI and MABr are dissolved in ethanol before being recrystallized from diethyl ether and dried at 60°C in a vacuum oven for 24 h. The prepared powders of PbI₂ and PbBr₂ for 0.8 M MAPb(I_{1-x}Br_x)₃ (x = 0.1-0.15) solution are stirred in a mixture of GBL and DMSO (7:3 v/v) at 60°C for 12 h. Using a continuous two-step spin coating process at 1,000 and 5,000 RPM for 10 and 20 sec respectively, the resulting solution is coated on top of the mp-TiO₂/bl-TiO₂/FTO substrate. In the second spin coating step, the substrate is treated with toluene drop casting (around 1×1 cm). A solution of poly (triarylamine) (15 mg, PTAA, EM Index, M_w = 17,500 gmol⁻¹) in toluene (1.5 mL) is mixed with 15 μL of a solution of lithium bistrifluoromethanesulphonimide (170 mg) in acetonitrile (1 mL) and 7.5 μL 4-tert-butylpyridine and spin-coated on the MAPb(I_{1-x}Br_x)₃ (x = 0.1-0.15)/mp-TiO₂/bl-TiO₂/FTO substrate at 3,000 RPM for 30 sec. Finally, an Au counter-electrode is deposited by thermal evaporation. The active area of this electrode is fixed at 0.16 cm².

The photovoltaic parameter result of this PSC is shown in Fig. 7 and Table 1. The J_{sc}, V_{oc} and FF values obtained from the I-V curve of the reverse scan are 19.2 mAcm⁻², 1.09 V and 0.69 respectively, yielding a PCE of 14.4% under standard AM 1.5 conditions. In contrast, the corresponding values from the I-V curve of the forward scan are 19.2 mAcm⁻², 1.07 V and 0.44 respectively, showing a pronounced discrepancy of 9.1% in overall efficiency. Certified power conversion efficiency up to 16.2% is achieved in this PSC (Jeon *et al.*, 2014).

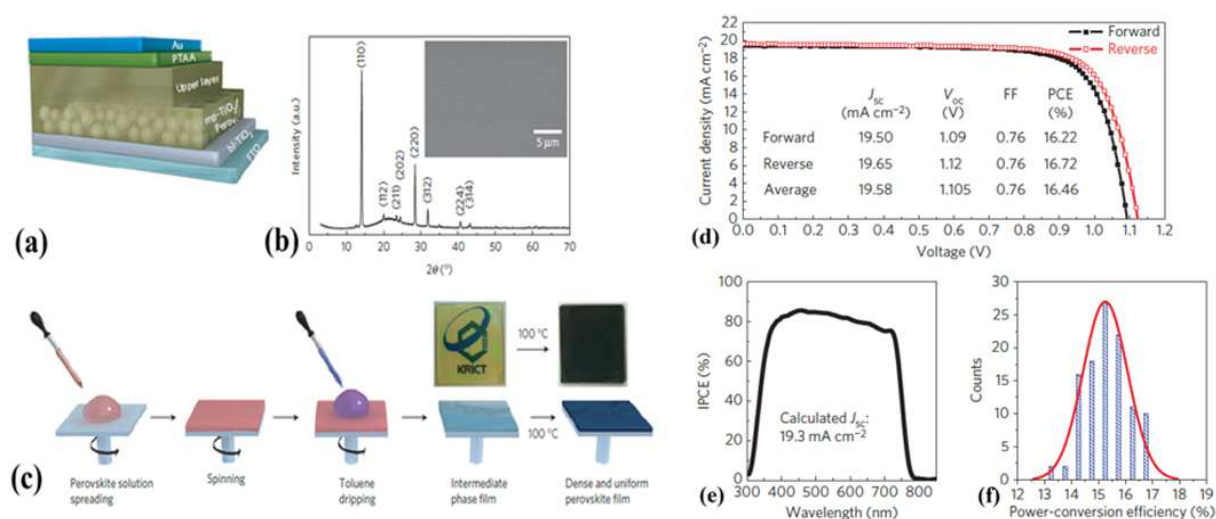


Fig. 7. (a) Device architecture of the bilayered perovskite solar cell (glass/FTO/bl-TiO₂/mp-TiO₂-perovskite nanocomposite layer/perovskite upper layer/PTAA/Au) (b) XRD pattern of the annealed perovskite coated on fused silica substrate. The inset shows a SEM image of a surface consisting of a glass/FTO/bl-TiO₂/mp-TiO₂-perovskite nanocomposite layer/perovskite upper layer (c) Solvent engineering procedure for preparing the uniform and dense perovskite film (d) J-V curves measured by forward and reverse scans, fabricated using a 200 nm-thick mp-TiO₂ layer (e) The IPCE spectrum for the best cell (f) Histogram of average efficiencies for 108 devices (Jeon *et al.*, 2014)

Table 1. Photovoltaic performance of perovskite solar cells without mp-TiO₂ or with 200-nm-thick mp-TiO₂ (Jeon *et al.*, 2014)

Device	Scan direction	J _{sc} (mA/cm ²)	V _{oc} (V)	FF	PCE (%)
W/O mp-TiO ₂	Forward	19.2	1.07	0.44	9.1
	Reverse	19.2	1.09	0.69	14.4
200-nm-thick mp-TiO ₂	Forward	20.1	1.08	0.73	15.8
	Reverse	19.9	1.06	0.75	15.9

Table 2. Different fabrication methods of HTM layer

HTM	Fabrication methods	References
Spiro-OTAD	Dissolve spiro-MeOTAD in chlorobenzene. Obtain 10% of (mole/mole) p-type doping of HTM by adding tris(2-(1H-pyrazol-1-yl)-4-tert butylpyridine) cobalt(III) bis(trifluoromethylsulphonyl)imide (FK209) into the solution. Spin coat on top of substrate.	Ramos <i>et al.</i> (2014)
	Add 1 mL of chlorobenzene with 0.70 M solution of Spiro-MeOTad with Li-TFSI and t-BP as additives. Spin coat on top of substrate with speed of 2000 rpm for 30 s. Store the device in the dark condition for overnight to dry the layer. To complete the fabrication of solar cell, gold electrodes will be deposited by thermal evaporation with thickness of 100 nm.	Sheikh <i>et al.</i> (2015)
	The solution can be prepared under N ₂ condition. Mix 10 wt.% of Co(III) complex (FK-102) in a solution of Spiro-MeOTAD (2,2',7,7'-tetrakis (N, N-di-p-methoxyphenylamine)-9,9'-spiro bifluorene) in chlorobenzene (120 mg mL ⁻¹). Add 24 μL of lithium bis(trifluoromethanesulfonyl)imide dissolved in acetonitrile (520 mg mL ⁻¹) and 37 μL of ter-butylpyridin. Spin coat the solution on the perovskite layer for 30 s with speed of 4000 rpm. Deposit the surface with 100 nm of gold by thermal evaporation and let it dry.	Li <i>et al.</i> (2015)
Polymer	2,2',7,7'-tetrakis-(N, N-dipmethoxyphenylamine) 9,9'-spirobifluorene (Spiro-MeOTAD) will spin coated on top of substrate with 2000 rpm for 60s under ambient condition. Leave the device in a closed box with silica desiccant for overnight in air.	Zhang <i>et al.</i> (2015) Di Giacomo <i>et al.</i> (2014)
	Use P3HT and copolymer P. Spin coat the HTMs polymer using HTMs solution in chlorobenzene on top of substrate with speed of 2500 RPM for 30 sec. Leave the device to dry for 1 h. Mix P3HT solution with dichlorobenzene (10 mg mL ⁻¹). Spin coat the solution on the substrate at 1500 rpm for 60 sec. On top of the HTM layer through shadow mask deposit a gold anode with the thickness of 220 nm.	Nagarjuna <i>et al.</i> (2015) Zhang <i>et al.</i> (2015)

Synthesis of HTM

The type of layers on top of the substrates, namely the Electron Transport Layer (ETL) and Hole Transporting Layer (HTL), is an important consideration in the fabrication of solar cell. These layers will facilitate the movement of holes and electrons around the device, thus a good choice in the fabrication of these layers will increase the efficiency of the PSC. From Table 2, one can observe that most of the fabrication methods of HTM layers are almost similar. Besides that, this table is useful to find the suitable method for the fabrication of HTM layer (either polymer or spiro-OTAD).

Summary of Fabrication Methods

Fabrication plays an important role in development of PSC and The summary of fabrication methods and chemicals are shown in Table 3. Based on Table 3, one can deduce that spin coating plays a major role in the fabrication of PSC.

Impact of Various Factors on PSC Performance

Despite the high efficiency of PSC, it still faces several challenges such as instability and some other

issues, thus researches are going on to explore the effect of those issues on the performance of PSC. In this section, a review on the different impacts of various factors such as atmosphere condition, film thickness and properties, HTM, electron transport, external electric field, blocking layer, transport layer, CBO and VBO absorber layer, heat treated ion assisted film, thermal annealed effect, reduced graphene oxide, blade coating and low temperature solution on the performance of PSC.

Impact of Storage Conditions on PSC Performance

In this section, the impact of varying storage conditions on the photovoltaic performance of TiO₂ CH₃NH₃PbI_{3-x}Cl_x spiro-OMeTAD solar cells will be analyzed. The results of the PSC performance under different dark storage conditions are summarized in Table 4. Based on the results shown in Table 4, it is apparent that the dry air is the most affordable storage condition to accomplish high energy conversion efficiency during the first few hours. Precursor composition, perovskite morphology, pore filling and processing temperature are significant factors in evaluating the solar cell efficiency. During the initial couple of hours, dry air is the most suitable storage condition for high energy conversion

efficiency. Ambient atmospheric condition, proper oxidization and p-doping spiro-OMeTAD are important elements that need to be considered during the drying process as it is tightly related to efficiency. To achieve efficiency of 15%, TiO₂ and spiro-bi fluorine have to be used as the electron collector and hole conductor respectively. Absence of oxygen during the drying process

can lead to decrement and increment in the electron conductivity and the recombination of charge carrier respectively. Electron conductivity of the LiTFSI-doped spiro-OMeTAD increases by two orders of magnitude when it is exposed to dry air. Some of the other factors that have been improved relatively to dry N₂ and vacuum conditions are photo-current density, FF and PCE.

Table 3. Summary of fabrication methods of PSC

PSC	Fabrication techniques				References
	Dipping	Spin coating	Spray pyrolysis	Thermal evaporation	
CH ₃ NH ₃ PbI _(3-x) /P3HT/Ag/Au CH ₃ NH ₃ PbI _{3-x} Cl _x	TiCl ₄ aqueous solution at 70°C for 30 min	TiO ₂ nanoparticles, P3HT in chlorobenzene solution TiO ₂ (2000RPM, 60 s) Dimethylformamide (DMF) solution (2000 rpm, 60 s)	At 470°C	Ag(10 nm)/Au(40 nm)	Ogomi <i>et al.</i> (2014)
CH ₃ NH ₃ I	-	Dyesol paste (5000 RPM, 30 s)	Titanium diisopropoxide bis(acetyl acetonate) at 450°C	-	Wang <i>et al.</i> (2015); Sheikh <i>et al.</i> , 2015; Di Giacomo <i>et al.</i> , 2014)
CH ₃ NH ₃ PbI ₃	-	CH ₃ NH ₃ PbI ₃ , PbI ₂ in N, Ndimethylformamide in 70°C	TiO ₂ deposited on the FTO glass	-	Ramos <i>et al.</i> (2014)
CH ₃ NH ₃ PbI ₃ /C ₄ H ₆ O ₂	-	30 mM tetrabutyl titanate in isopropyl alcohol (500 RPM, 15 s)	-	-	Xin <i>et al.</i> (2014); Woojun <i>et al.</i> , 2014)
PbI ₂ + CH ₃ NH ₃	CH ₃ NH ₃ I in anhydrous isopropanol 10 mg mL ⁻¹	PbI ₂ in N, Ndimethylformamide, 460 mg mL ⁻¹ heated at 60°C (3000 rpm, 40 s)	compact TiO ₂	-	Xiao <i>et al.</i> (2014)
K ₂ La ₂ Ti ₃ O ₁₀ doped by aqueous NH ₃ solution	-	-	-	-	Razza <i>et al.</i> (2015)
CH ₃ NH ₃ PbI ₃ -TiO ₂ NCS	8 mg mL ⁻¹ CH ₃ NH ₃ I	0.554 g mL ⁻¹ PbI ₂ in N, N-dimethylformamide (DMF)	-	-	Huang <i>et al.</i> (2010)
CH ₃ NH ₃ Pb _x	0.04 M TiCl ₄ in H ₂ O for 30 min	mesoporous TiO ₂ layer	thin layer of TiO ₂	Deposition of 80 nm thick gold	Zhong <i>et al.</i> (2015)
PZT-Terray Perovskites MoO ₃ -Au-MoO ₃	-	-	-	-	Sfyri <i>et al.</i> (2015)
MoO ₃ -Au-MoO ₃	-	1:1 M ratio of CH ₃ NH ₃ I and PbI ₂ Spiro-OMeTAD (3000 rpm, 30 s)	-	Dissolving 41.6 mg Spiro-OMeTAD, 7.5 μL of a stock solution of 520 mg mL ⁻¹ LiTFSi in acetonitrile and 16.9 μL TBP in 0.5 mL chlorobenzene	Wasa <i>et al.</i> (2016)
CsXMA1-XPbI ₃	-	Equimolar amounts of CsI:CH ₃ NH ₃ I and PbI ₂ in a mixed solvent consisting of 120 mg mL ⁻¹ DMF: GBL (97:3 [vol%])	-	-	Della Gaspera <i>et al.</i> (2015)
CH ₃ NH ₃ PbI _{3-x} Cl _x (= MAPbI _{3-x} Cl _x)	-	TiO ₂ films at 2500 RPM for 30 s, in argon-filled glove box	-	-	Choi <i>et al.</i> (2014)
Zo-PET and CH ₃ NH ₃ PbI ₃	-	Titania suspension onto IZO-PET at 2000 rpm for 60 s	-	-	Li <i>et al.</i> (2015); Zhang <i>et al.</i> , 2015)
					Dkhissi <i>et al.</i> (2015)

Table 4. Photovoltaic parameters of the solar cells stored under disparate environmental conditions (Sheikh *et al.*, 2015)

Dark storage condition	J _{sc} (mA/cm ²)	V _{oc} (V)	FF (%)	PCE (%)
Vacuum	12.2	0.77	57.5	5.4
Dry air	18.4	0.89	68.9	11.2
Dry nitrogen	13.4	0.80	67.7	7.2

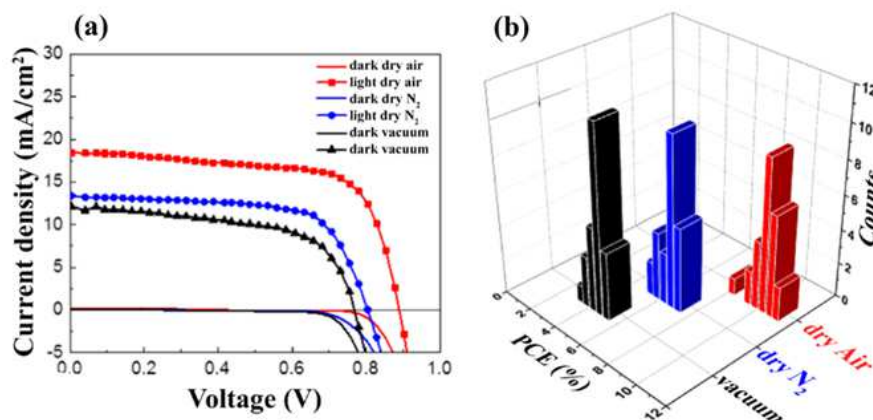


Fig. 8. (a) J-V characteristic curve and (b) Histograms of the PCE (%) data for the treated PSCs (24 samples for each of the three sets) (Sheikh *et al.*, 2015)

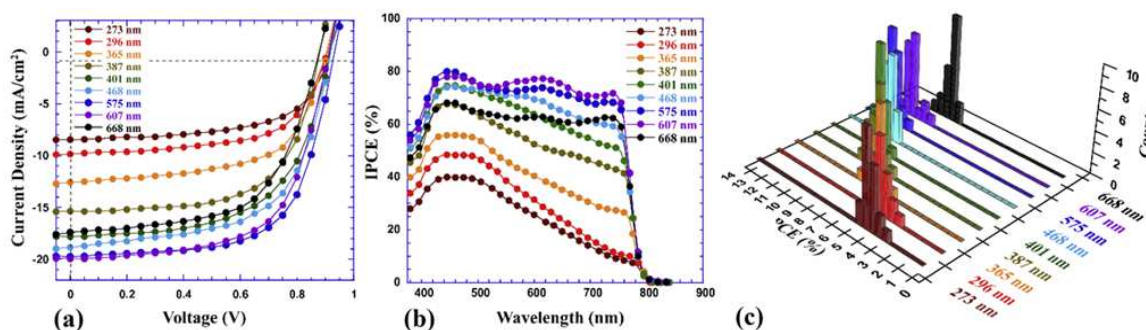


Fig. 9. (a) J-V characteristics of PHJ perovskites hybrid PSC with disparate thickness layer of $\text{CH}_3\text{NH}_3\text{PbI}_{3-x}\text{Cl}_x$ (b) IPCE spectra of pero-HSCs (c) Comparison of histograms of efficiencies of pero-HSCs perovskites with varying film thickness (Wang *et al.*, 2015)

The performance graphs of three solar cells treated under different dark storage conditions are shown in Fig. 8. The charge carrier density is enhanced with high resistivity and p doping. As mentioned before, long term stability is a big issue in PSC and this concern can only be minimized by keeping the device away from detrimental moisture and by encapsulation process after proper oxidation of HTM. Fermi level of the spiro-OMeTAD becomes lower due to the light illumination and this will result in higher V_{OC} . The highest efficiency of 11.2% is achieved under dry air condition, whereas the efficiency is only 5.4 and 7.2% under vacuum and dry N_2 conditions respectively. Furthermore, PSC stored under dry air condition has the highest open circuit voltage of 0.89 V, highest photo-current density of 18.4 mA/cm^2 and largest fill factor of 68.9%. Although the PSC stored in dry air exhibits a marginally better performance than PSCs stored under dry N_2 and vacuum conditions, the atmospheric gas storage condition does not have much effect on the final efficiency. Besides, the light harvesting efficiency remains generally the same under different storage conditions (Sheikh *et al.*, 2015).

Impact of Film Thickness on PSC Performance

Even though a considerable amount of literature on the on performance of perovskite has been published, the correlation between the film thickness of $\text{CH}_3\text{NH}_3\text{PbI}_{3-x}\text{Cl}_x$ (hybrid) perovskite layers and its performance are rarely addressed. As shown in Fig. 9a and 9b, the effects of $\text{CH}_3\text{NH}_3\text{PbI}_{3-x}\text{Cl}_x$ film thickness on both J_{SC} and PCE are moderate when the thickness of $\text{CH}_3\text{NH}_3\text{PbI}_{3-x}\text{Cl}_x$ film is larger than 400 nm. When the film thickness is decreased to around 200 nm, both J_{SC} and PCE are improved by 15 and 37%, respectively. Photo-responses below 500 nm are moderately enhanced in comparison with photo-responses in the wavelength region from 550 to 800 nm, which are dramatically enhanced. Minimization of the surface charge carrier recombination due to the enlarged surface coverage leads to the reduction of energy loss. Efficiencies of PHJ pero-HSCs are heavily depending on the film morphology of $\text{CH}_3\text{NH}_3\text{PbI}_{3-x}\text{Cl}_x$ layer when the film thickness is larger than 400 nm. Based on Table 5, due to the large surface roughness in the films thicker than 600 nm, both J_{SC} and PCEs will decrease. From Table 5, the relationship

between the efficiencies of “planar heterojunction” and the thin film thicknesses, as well as the morphologies of solution-processed $\text{CH}_3\text{NH}_3\text{PbI}_{3-x}\text{Cl}_x$ perovskite layers can be observed (Wang *et al.*, 2015).

In Table 6, the performance results are based on TiO_2 thin films with different film thickness for quantum dot sensitized PSCs. As long as the absorption coefficient of quantum dots perovskite is high, the photo-current density of thinner films will be relatively higher compared to thicker films. By controlling the concentration of coating solution, post-annealing condition and TiO_2 surface modification on the quantum dot PSC, the efficiency of 6.54% can be achieved at AM 1.5G 1 sun illumination, as presented in Table 6. Because quantum dot tends to dissolve constantly into the redox electrolyte, one big issue of $(\text{CH}_3\text{NH}_3)\text{PbI}_3$ quantum dot sensitized solar cell is its stability. It is stable for approximately 10 min (about 80% degradation) under continuous irradiation (Im *et al.*, 2011). As shown in Table 7, the performance of the device is extremely well. This device has an eminently reproducible V_{OC} and it is in the excess of 1.0 V. The average current density of this short circuit (J_{SC}) is nearly 20 mA cm^{-2} , with an average PCE of 13.7% and a very good fill factor of 70% (Liu and Kelly, 2014).

Impact of Superior Grain Growth and Light Harvesting Properties on PSC Performance

Another approach to improve the efficiency of PSC is by supervising the grain growth and light harvesting properties. The performance of PSC cells made of nano-assembled TiO_2 structure dispensed on TiO_2 compact layer, integrated with PbI_2 or $\text{CH}_3\text{NH}_3\text{PbI}_3$ layers, are shown in Fig. 10. Because of the relatively smoother, nano-grained nature of the surface of PbI_2 , perovskite crystal size is smaller in case of TiO_2 NP. Larger perovskite crystallites also can enhance light scattering and reduce recombination at the $\text{TiO}_2/\text{CH}_3\text{NH}_3\text{PbI}_3/\text{HTM}$ interface. Higher amount of PbI_2 retained on the TiO_2 NB film can lead to enhanced grain growth of perovskite crystallites in the NB case and result in poor performance. Efficiency improvement using NB cell can be observed in the increment in both J_{SC} and V_{OC} . Performance of the PSC can be enhanced (based on Table 8, efficiency increases about 17%) by using NBs, in addition of a striking improvement of the grain size. Larger V_{OC} in NB cell is attributed to the larger $\text{CH}_3\text{NH}_3\text{PbI}_3$ crystal size, which leads to the reduction in the grain boundary density (Tathavadekar *et al.*, 2015).

Table 5. Parameters of perovskites hybrid solar cells supported on solution-processed $\text{CH}_3\text{NH}_3\text{PbI}_{3-x}\text{Cl}_x$ films with different thicknesses (Della Gaspera *et al.*, 2015)

Thickness of $\text{CH}_3\text{NH}_3\text{PbI}_{3-x}\text{Cl}_x$ layer (nm)	PCE (%)	FF	V_{OC} (V)	J_{SC} (mA/cm ²)
273±10	4.88±0.52	61.2±0.8	0.95±0.02	8.45±0.56
296±13	5.64±0.48	61.8±0.6	0.93±0.04	9.82±0.63
365±18	7.18±0.47	61.3±1.0	0.93±0.04	12.60±0.75
387±15	8.61±0.52	62.2±0.7	0.90±0.07	15.38±0.58
401±16	9.84±0.55	61.0±0.9	0.93±0.03	17.34±0.64
468±14	10.72±0.48	61.2±0.8	0.93±0.04	18.84±0.59
575±14	11.88±0.44	63.2±0.4	0.95±0.02	19.79±0.41
607±17	11.82±0.51	63.7±0.5	0.93±0.06	19.96±0.44
668±21	9.42±0.45	60.0±0.7	0.91±0.06	17.26±0.69

Table 6. Performance parameters of quantum dot sensitized PSC with different TiO_2 film thickness (Im *et al.*, 2011)

TiO_2 film thickness	J_{SC} (mA/cm ²)	V_{OC} (V)	FF (%)	η (%)	Area (cm ²)
3.6	15.99	0.629	0.617	6.20	0.309
5.5	14.31	0.616	0.589	5.19	0.284
8.6	10.15	0.559	0.594	3.37	0.277

Table 7. Performance parameters of PSC with varying ZnO film thickness (Liu and Kelly, 2014)

No of layers	ZnO film thickness	J_{SC} (mA/cm ²)	V_{OC} (V)	FF (%)	PCE (%)
0	0	16.5	0.46	31.7	2.4
1	10	18.0	0.99	62.4	11.1
3	25	20.5	1.01	69.6	14.4
5	40	18.9	1.01	70.0	13.3
8	70	18.4	1.01	69.5	12.9

Table 8. Solar cell parameters for the NP and NB cell on PSC (Tathavadekar *et al.*, 2015)

Device	η (%)	FF (%)	V_{OC} (V)	J_{SC} (mA/cm ²)
NB cell	9.0	0.52	0.99	17.4
NP cell	7.7	0.65	0.9	13.1

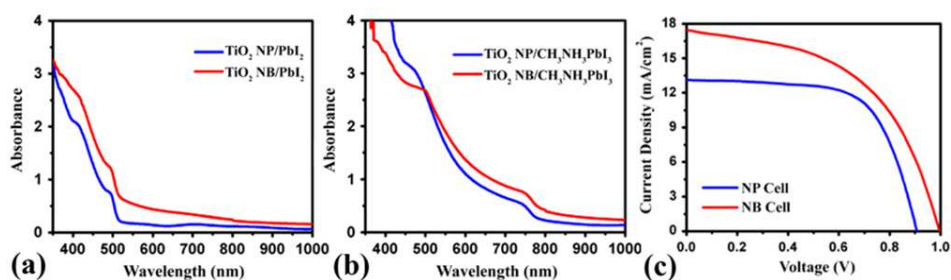


Fig. 10. UV-vis absorbance spectra of (a) PbI_2 -loaded and (b) $\text{CH}_3\text{NH}_3\text{PbI}_3$ -loaded TiO_2 (NP and NB) films on FTO substrate respectively (c) J-V characteristic curves for NP cell and NB cell (Tathavadekar *et al.*, 2015)

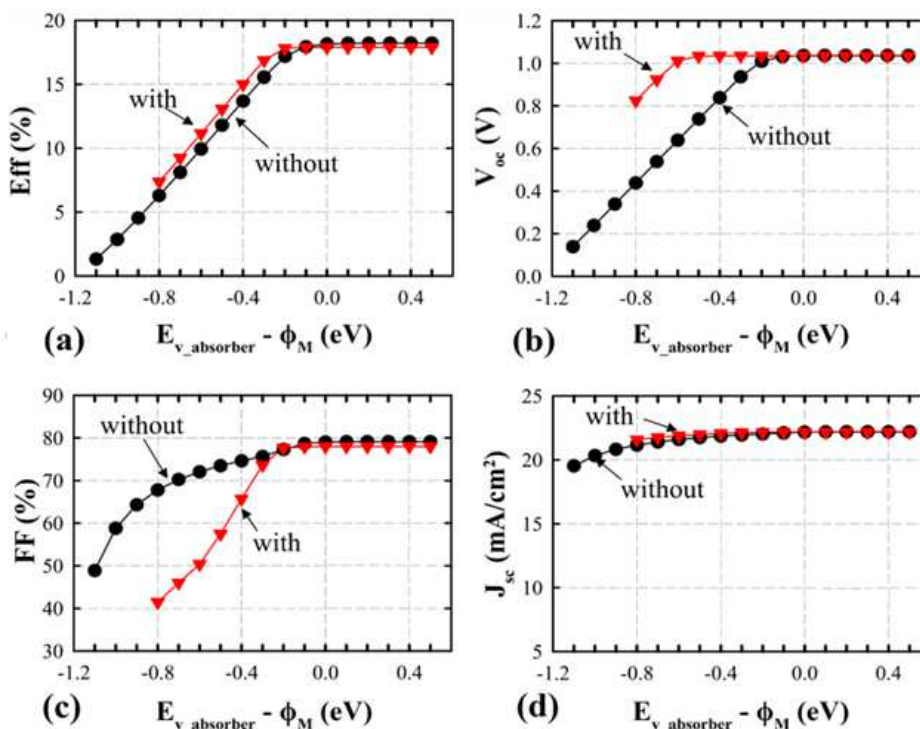


Fig. 11. Parameters of PSCs with and without HTM as a function of $E_{v_absorber} - \phi_M$ (Minemoto and Murata, 2014)

Impact of Hole Transport Material (HTM) on PSC Performance

Although HTM can contribute to the efficiency, it cannot resolve the problem of ϕ_M mismatching. Presence of the HTM will increase the amount of V_{BI} and thus the elimination of HTM is required to preserve the stability of the device. Nonetheless, to achieve a high efficiency, elimination of mesoporous layer is necessary. Improvement of the absorber quality, the matching of ϕ_M and back contact material are essential for further improvement of device performance. In open circuit, the monotonical decrease in V_{BI} leads to the decrease in the circuit voltage and reduction of electric field across the absorbance. By moving ϕ_M upward to vacuum level, both V_{OC} and FF will decrease, as shown in Fig. 11. Exclusive of the presence of HTM, the choice of the

back contact material is critical in achieving high efficiency. Indicating the ϕ_M matching is one of the requirements for achieving high efficiency up to 17.9% (Minemoto and Murata, 2014).

Impact of Compact Layer (CL) Thickness on PSC Performance

In this section, the influence of the CL thickness on disparate electron transport path in perovskite is investigated. Generally, increase in the thickness of the CL will improve the performance of the device. Decrease in the area of contact is the reason for the suppression of the electron transport from FTO to HTM and HTM and FTO electrodes form ohmic contacts, leading to the recombination of charge carriers. When the thickness of CL is increased, J_{SC} , V_{OC} and η of

device will be increased also. The graph in Fig. 12 indicates that the optimal perovskite performance can be achieved at CL thickness of 90 nm. However, there is a reduction in transparency at 90 nm CL and reduction in transmittance at the thickness of 180 nm. Any further increment in the CL thickness will reduce the recombination retardation and lead to poor performance. Higher optical transmittance allows improvement in absorbance of light, which in turn increases the number of excited electrons. As shown in Table 9, cells with thicker CL have lower current and cells without CL have low energy conversion efficiency.

The CL thickness dependency varies in three sets of fabricated solar cells: FTO/CL/nc-TiO₂/Perovskite/HTM/Carbon (1; classical cell), FTO/CL/ncTiO₂/Perovskite/Carbon (2; omitting HTM) and FTO/CL/Perovskite/HTM/Carbon (3; omitting nc-TiO₂). Figure 12a-d present the photovoltaic characteristics of these three sets. The smoothest TiO₂ layer is at the thickness of 90 nm and at the thickness of 180 nm there will be a decrement in the transmittance, while at 390 nm there will be 20% decrement in the transmittance. To achieve a high performance for solar cell, the thickness should be less than 180 nm. A continuous layer can be formed by tightly coating a CL on the FTO (Wang *et al.*, 2014a).

Impact of External Electric Field on Planar Heterojunction PSC Performance

By operating at a low temperature, planar heterojunction PSC can be fabricated. Figure 13 and 14 illustrate the performance of PSCs under different bias scanning range and different external bias respectively. Performance of this solar cells is strongly reliant on the external bias, while the light soaking effect is inconsequential.

By the appropriate optimization of the bias conditions, power conversion efficiency can be increased by 8-fold. Besides, PCE can increase significantly from 1% to over 8% by applying an external bias prior to the device measurement. Larger scan bias range means better performance (From 0.13%

at -1 to 1 V to 4.29% at -1 to 6 V). But when the range is too high (for instance 1 to 8 V), the device may get destroyed due to the large injection of current density and eventually, as a result the performance will degrade. Another factor that can lead to decrement in performance is negative bias. On the other hand, positive bias leads to the increase in the performance of PSC. The reproducibility and stability of the device will be increased if ionic transport decreases. There are three possible reasons that can explain the dependency performance on external bias, which are the trap states in perovskite, ferroelectric nature of perovskite and ionic transport in perovskite (Li *et al.*, 2015).

Impact of Blocking Layer on Organic Metal Halide PSC Performance

To form the blocking layer, titanium precursor solution, which is fabricated either by spin coating, spray pyrolysis or atomic layer deposition, is used. Addition of a compact electron blocking layer will prevent charge recombination originated in FTO and the hole conducting layer, thus ensuring an effective charge. Compact and appropriate thickness of the electron BL can lead to increase in the conductivity and photovoltaic performance. In addition, it can ensure the film uniformity of PSC. For high energy conversion efficiency, a highly compact BL film is very critical. Spin coating the precursor solution of TTIP and then PTA will increase the performance of the solar cell, nevertheless the pinholes within the compact layer will pose negative effect on the performance. As shown in Fig. 15a, the diffraction intensity will be affected if the thickness of the film that is generated by PSP is thicker than that of SP and PS. The device performance will have much improvement (based on Table 10, J_{SC} of 12.96 mA cm⁻² and V_{OC} of 0.738 V together with FF of 48.77%), after performing spin coating of the precursor solution of PTA on the BL film of PS. This will reveal the importance of the BL in the device. Blocking layer can ensure that an effective charge can be extracted by preventing the hole conducting layer (Jianping *et al.*, 2014).

Table 9. Performance parameters of PSC with varying thickness of compact TiO₂ layer (Wang *et al.*, 2014a)

No. of spraying cycles	Layer thickness (nm)	V _{OC} (V)	J _{SC} (mA/cm ²)	PCE (%)	FF (%)
0	No compact layer	0.87	5.59	1.34	0.274
2	20	0.92	6.73	1.65	0.266
4	90	0.93	12.18	3.17	0.279
10	180	0.87	9.88	2.87	0.335
20	390	0.89	9.29	1.93	0.232

Table 10. Photovoltaic parameters of PSCs based on disparate BL films (Jianping *et al.*, 2014)

Cell	V _{OC} (V)	J _{SC} (mA/cm ²)	η (%)	FF (%)	RS (ohm)
PS	0.515	10.52	2.21	40.87	124.07
SP	0.709	13.32	5.51	54.57	84.04
PSP	0.738	12.96	4.66	48.77	109.57

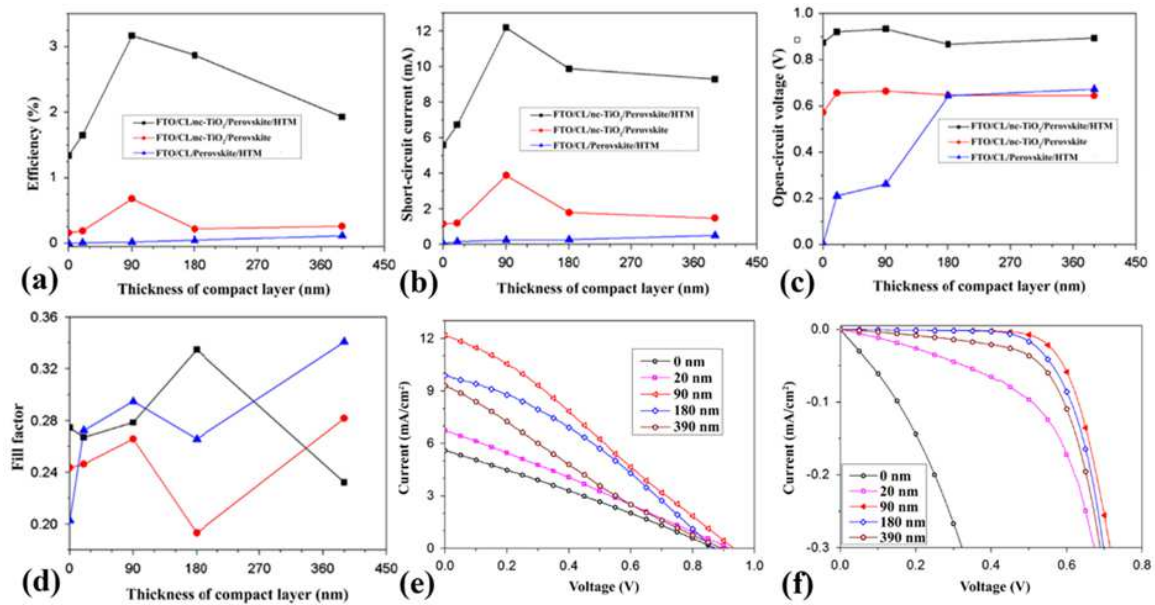


Fig. 12. (a) Power conversion efficiency (η) (b) Short-circuit current density (J_{sc}) (c) Open-circuit voltage (V_{oc}) (d) Fill factor (FF), J-V characteristics under (e) Light and (f) dark conditions of PSC containing compact TiO_2 layers of different thicknesses (Wang *et al.*, 2014a)

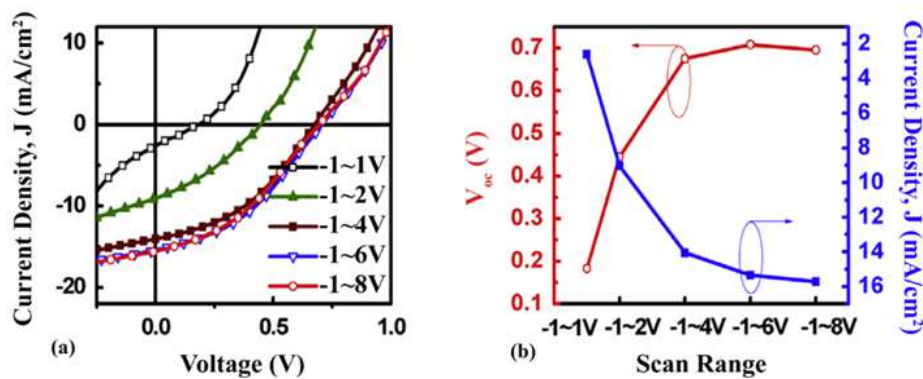


Fig. 13. (a) J-V curves and (b) V_{oc} and J_{sc} values under different scan bias range. The scans are from the positive bias to negative bias (Li *et al.*, 2015)

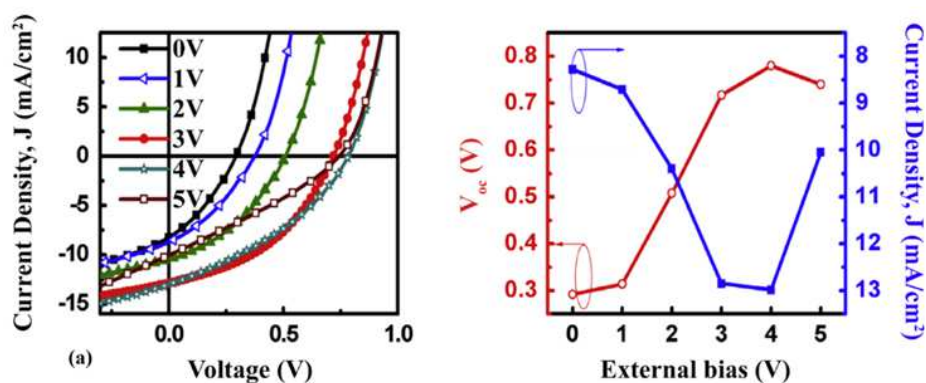


Fig. 14. (a) J-V curves and (b) V_{oc} and J_{sc} values under different external bias for 30 s using the same scan range (0.5 to 1.5 V) (Li *et al.*, 2015)

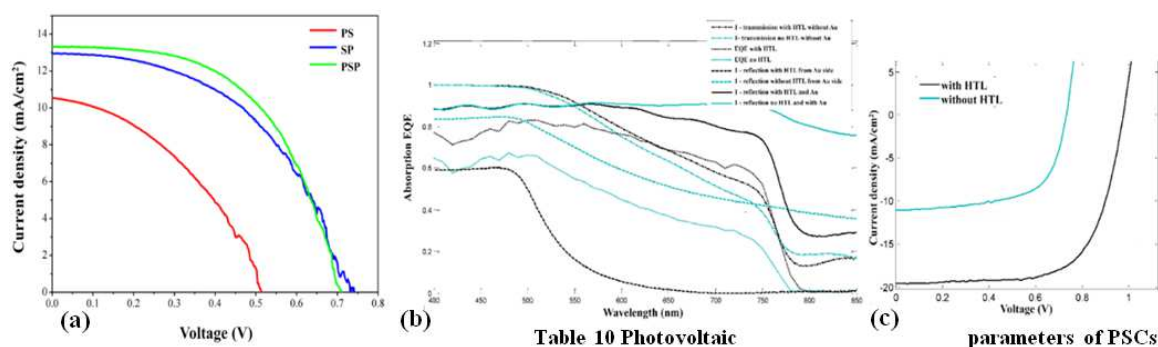


Fig. 15. (a) J-V curves based on different BL films (Jianping *et al.*, 2014) (b) Absorption spectra of a device with and without HTL (c) Current voltage curves of devices with and without HTL (Tress *et al.*, 2014)

Impact of Hole Transparent Layer on PSC Performance

In this section, the influence of hole transparent layer in CH₃NH₃PbI₃ PSC will be discussed. Generally, hole transparent layer is valuable because it exhibits better charge carrier collection efficiency. However, it also increases and decreases V_{OC} and recombination respectively. Selectivity of contact in the layer increases due to the recombination at the hole collection electrodes. As shown in Fig. 15b and 15c, at the band edge of perovskite (wavelength 750 to 800 nm) absorption will drop strongly, but for the small wavelength (less than 500 nm), absorption will decrease gradually. At wavelengths below 500 nm, the absorption is unity for the both PSCs with and without HTL and because of the constant ratio on the EQEs around this wavelength range, the internal quantum efficiency will have to be changed, i.e., charge carrier collection efficiency. For the device without HTL it is decreased by 18% (3.5 mA/cm²) (Tress *et al.*, 2014).

Impact of Conduction Band Offset (CBO) and Valence Band Offset (VBO) on PSC Performance

Interface recombination will become prominent due to the high reduction of activation energy when the valence band energy of absorber layer is higher than the conduction band energy of buffer layer. As a result, the spike formed by the CBO will serve as a fence for photo-generated carrier flow. Figure 16a-d show the performance parameters of PSC with varying CBO, VBO and interface defect density values. High value of CBO induces double-diode-like curvature and leads to low FF and stable V_{OC}. When CBO decreases from 0.0 to -0.4 eV, fill factor will be decreased while J_{SC} remains almost unchanged. Negative CBO reduces V_{OC} and V_{OC} corresponding to E_a, however it will increase the interface recombination. From here, open circuit states that the conduction band of the buffer is at least equal or higher than the amount of the absorber.

Low and high VBO have the same hole concentrations, but high VBO means poor FF. Negative VBO decreases both V_{OC} and FF, but J_{SC} will stay almost unchanged. Increase in VBO will decrease FF and electric field across the absorber. In the similar situation, prominent increase in the interface recombination will happen due to the higher position of the valence band of the HTM in relative to the absorber. Too low position for the valence band of HTM leads to the incomplete depletion of the absorber. Based on the results, the optimum conduction and valence band energy of buffer and HTM are 0.003 eV higher and 0.002 eV lower than the corresponding bands of absorber respectively. These results are essential guidelines in designing new buffer, absorber and HTM (Minemoto and Murata, 2015).

Impact of Heat Treated Films, Ion-Assisted Films and Thermal Annealing on PSC Performance

Heat treated films and ion assisted films can be used to accelerate the reaction between CH₃NH₃I and PbI₂. By annealing a better crystallinity and high phase purity can be obtained, however with ion assisted greater amorphous structure will be obtained, also different morphologies of grown thin films will be created. Table 11 presents the performance data of PSC with varying annealing time. After heat treating, optical properties, crystallinity and phase purity of the solar cell will increase in more stable film. Phase purity of perovskite can be achieved by only use of ion assisted deposition, without the help of post deposition heat treatment. There is a relation between beam energy and crystallinity of the film, without the ion beam irradiation the crystallinity of film decreases, however the decrease in the beam energy increases the crystallinity of the resultant film. Besides that, by using heat a solar cell with better crystallinity and high phase purity can be achieved, while greater amorphous structure will be achieved with ion assisted process. Different morphologies of grown thin films can also be fabricated (Cimaroli and Yanfa, 2014). In order

to improve the device performance, the $\text{CH}_3\text{NH}_3\text{PbBr}_3/\text{ZC-NA}$ composite is annealed at 80°C . After the thermal annealing, while the V_{OC} remains unchanged, there is a slight increase in J_{SC} and fill factor and that leads to improvement in averaged η (increases from 3.34% up to 4.31% under AM 1.5 illumination (100 mW/cm^2)). As shown in Fig. 17a, the drop in transmittance at 800 nm is indicative of the direct band gap of the perovskite. Some of the other effects of thermal annealing are such as stabilizing the presence of $\text{CH}_3\text{NH}_3\text{PbBr}_3$ crystals and improvement of device performance. Enhancing the crystallinity and reducing the charge recombination will increase the charge transport properties of the perovskite (Boix *et al.*, 2014).

The performance data shown in Table 12 is obtained under one sun illumination (100 mWcm^{-2}) at AM1.5 G condition from 40.26 wt%, using equimolar mixture of $\text{CH}_3\text{NH}_3\text{I}$ and PbI_2 in *g*-butyrolactone. The electrolyte composition is 0.9 M LiI, 0.45 M I_2 , 0.5 M tBP and 0.05 M urea in ethyl acetate. Photovoltaic property can be adjusted to certain extent by manipulating the annealing temperature. Photovoltaic performance of 5.5 mm-thick TiO_2 layer is slightly improved from voltage of 0.6046 V, photo-current of 13.31 mA/cm^2 and fill factor of 0.5013 to 0.6172 V, 13.76 mA/cm^2 and 0.557 respectively, as presented in Table 12. This improvement is due to the increase of the annealing temperature to 100°C (Im *et al.*, 2011).

Table 11. Photovoltaic parameters with varying annealing time on PSC (Song *et al.*, 2015)

Annealing time (min)	J_{SC} (mA/cm^2)	V_{OC} (V)	FF (%)	η (%)
40	19.35	0.978	68.94	13.04
55	19.64	1.018	70.04	14.00
70	19.37	1.033	70.37	14.08
90	19.82	1.038	71.15	13.89
110	18.15	1.024	69.15	12.85

Table 12 Influence of annealing temperature on short-circuit performance of quantum dot PSC (Im *et al.*, 2011)

Annealing temperature ($^\circ\text{C}$)	TiO_2 film thickness	J_{SC} (mA/cm^2)	V_{OC} (V)	FF (%)	η (%)	Area (cm^2)
40	5.5	13.31	0.605	0.513	4.13	0.265
100		13.76	0.617	0.557	4.73	0.267
160		10.06	0.627	0.588	3.71	0.303

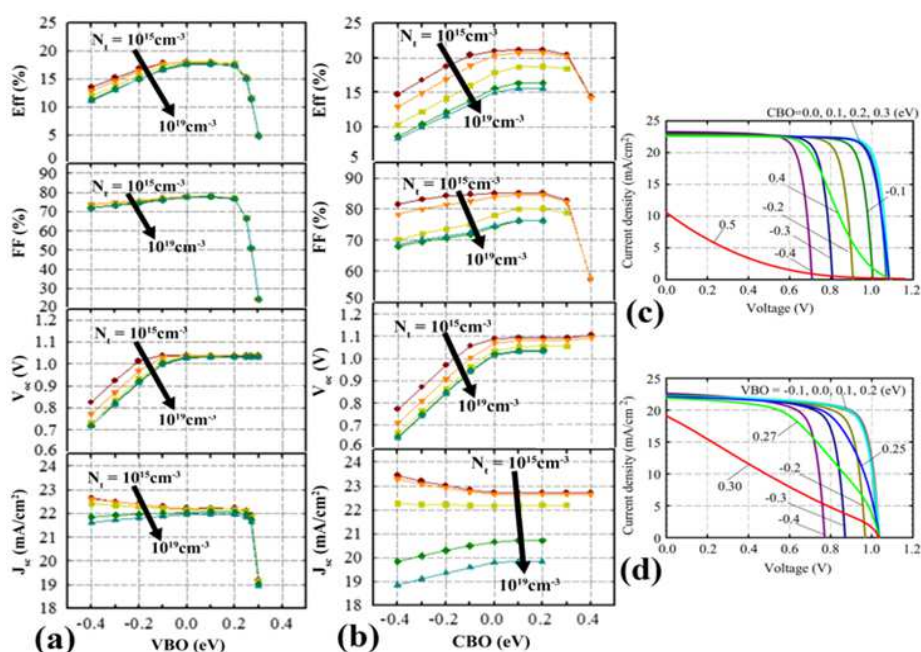


Fig. 16. (a) Parameters of PSC with CBO of the buffer/absorber interface set to zero (b) Parameters of PSC with disparate interface defect densities as a function of CBO of buffer/absorber interface, with VBO of the absorber/HTM interface set to zero (c) J-V curves with the interface defect density of IDL1 set to 10^{16} cm^{-3} (d) J-V curves of PSC with disparate VBO values of absorber/ HTM interface, with CBO of the buffer/absorber interface set to zero and the interface defect density of IDL2 set to 10^{16} cm^{-3} (Minemoto and Murata, 2015)

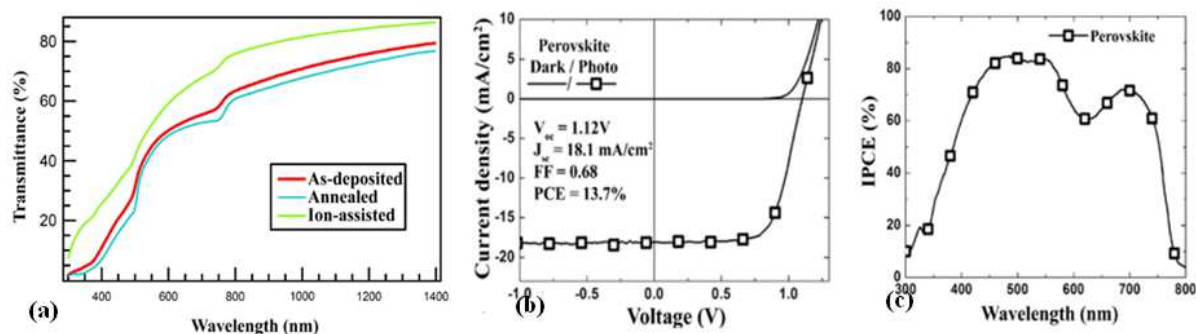


Fig. 17. (a) UV -Vis transmittance spectra of the as-deposited annealed and ion-assisted CH₃NH₃PbI₃ thin films (Boix *et al.*, 2014) (b) The J-V characteristic curve and (c) IPCE spectrum of the best performing PSC that employs MoO₃/NPB layer as hole extraction layer under fully vacuum processing conditions. The scan step of J-V characteristics is 0.02 V with 0.3 s of interval time for each step and the scan direction is from negative to positive voltage (Kim *et al.*, 2015)

Impact of Buffer Layer on PSC Performance

The fundamental purpose of the buffer layer is to provide a layer between aqueous solutions for depositing HTM during solar cell preparation and also to absorb photons under photo-illumination. Buffer layer leads to weak light absorbance at the wavelength ranging from 550 to 600 nm and it will increase J_{sc} due to the ignorable attenuation effect. As a result, it can protect the solar cell from contacting with the solution (Liu *et al.*, 2015).

Impact of Varying Environmental Parameters on PSC Performance

Impact of Air Mass on PSC Performance

Generally, optical air mass is defined as the optical path length scale for the solar beam over the atmosphere to the optical path over a standard atmosphere at sea level, when sun is at the zenith position. Dry air molecules reduce this ratio to a purely geometrical value. Variation in air mass will lead to amplification or attenuation of solar irradiance, photon density distribution and strong absorption in the visible region. It should be noted that a considerable loss of air mass ratio will occur at AM 1.5. However, high AM will shift the photon distribution into shorter wavelength regions. The blue spectral region is where attenuation of AM is higher and where majority of absorption bands occur. This demonstrates the strict condition imposed by air mass on the performance of PSC (Senthilarasu *et al.*, 2015).

Impact of Aerosol Optical Depth (AOD) on PSC Performance

The small particles that are suspended in the air are called aerosol. The parameter used in measuring the atmospheric attenuation of solar radiation by aerosol is called the aerosol optical depth. Increase in the AOD will change the incoming irradiance. Due to improvement of turbidity due to increment in AOD,

there will be more attenuation and scattering of solar irradiance in the visible UV spectra. The narrow absorption band in the blue wavelength region of the spectrum will be more affected under the turbidity condition. If the aerosol concentration in the atmosphere is low, the spectral losses will be lower than the air mass condition and there will be no effect on the PSC performance (Senthilarasu *et al.*, 2015).

Impact of Perceptible Water on PSC Performance

The integrated amount of water vapor in zenith direction between the surface and the top of the atmosphere is called perceptible water. To be more precise, the thickness of the liquid water that would be formed if all the vapor in the zenith direction were condensed at the surface of a unit area is also described as the thickness of the liquid water. The improvement in PSC performance by increasing perceptible water, which results in the enhancement of absorption of solar radiation near the infrared spectra, can be observed (Senthilarasu *et al.*, 2015).

Impact of MoO₃/NPB as Hole Extraction Layers on Fully Vacuum Processed PSC Performance

Fully vacuum processed PSC will yield better reproducibility. Acceleration in the advancement of the PSCs, high V_{oc} and free from the restriction of their solvents are some other benefits of this process. Employing MoO₃/NPB layer as the hole extraction layer is the main reason which is responsible for the high V_{oc}. From Fig. 17, the best results that can be achieved under the aforesaid conditions are 13.7% for PCE, 18.1 mA/cm² for J_{sc}, 1.12 V for V_{oc} and 0.67 for FF. In Fig. 17c, the scan step of J-V characteristics is 0.02 V with 0.3 sec of interval time for each step and the scan direction is from negative to positive voltage. Vacuum processed PSC is a promising tool to apply the various charge transport materials in the layered structures (Kim *et al.*, 2015).

Impact of Poly (3-Hexylthiophene) Hole Transport Layer on High-Efficiency CH₃NH₃PbI_{3-x}Cl_x PSC Performance

One of the suitable HTM choices for high-efficiency PSC is doped P3HT. The performance of the fabricated device can achieve up to 9.3% PCE and high V_{OC}. As shown in Fig 18a, the black-colored line represents the absorbance of a dehydrated TiO₂ sample, while the dark-gray-colored line and the light-gray-colored line represent the absorbance of a UV-treated sample and a sample without any treatment respectively. The TiO₂ thickness is 700 nm and a 40% w/w perovskite precursor solution is spin coated at 2000 RPM and annealed at 120°C for 1 h. All measurements are carried out using an integrating sphere. Absorbance of FTO/glass has been subtracted from the absorbance spectra of all the samples. On the other hand, in Fig. 18b, the current density over voltage curves of the best FTO/c-TiO₂/nc-TiO₂/CH₃NH₃PbI_{3-x}Cl_x/P3HT/Au (red-colored line and symbols) and FTO/c-TiO₂/nc-TiO₂/CH₃NH₃PbI_{3-x}Cl_x/spiro-OMeTAD/Au (black-colored line and

symbol) solar cells are presented. The PSC efficiency can be further improved by replacing Al₂O₃ with TiO₂. Adjusting the perovskite composition through addition of Br or other elements also serves the same objective (Di Giacomo *et al.*, 2014).

Impact of Reduced Graphene Oxide (RGO) on Highly-Efficient and Stable Planar PSC Performance

RGO nano-sheets are used as electrode interlayer. A highly-efficient and stable CH₃NH₃PbI₃ PSC, high RGO conductivity, better aligned energy levels and better growth of the crystalline CH₃NH₃PbI₃ can be expected through the addition of the novel RGO HTM. PSCs with RGO have an excellent reproducible efficiency up to 10.8%. Researches have revealed that facilitated charge collection with retarded charge recombination, high RGO conductivity, better aligned energy level and better growth of crystalline CH₃NH₃PbI₃ on RGO HTMs are the reasons for improvement in the performance of PSCs with RGO HTM.

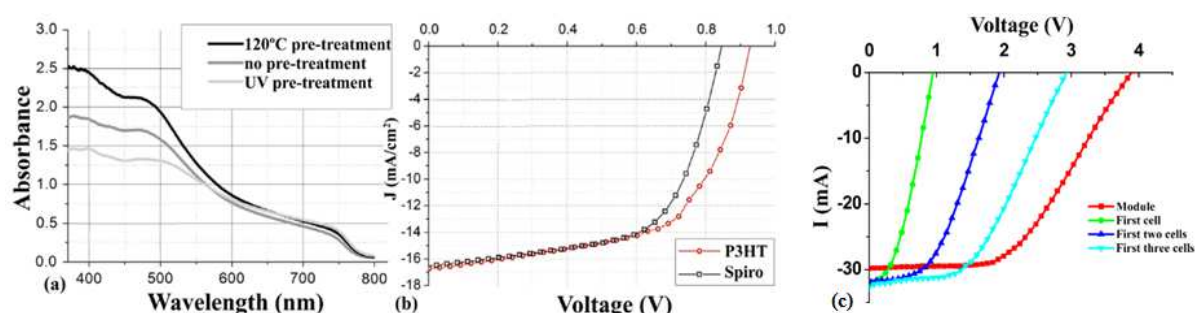


Fig. 18. (a) Absorbance spectra of TiO₂/CH₃NH₃PbI_{3-x}Cl_x on FTO glass (b) J-V curves of FTO/c-TiO₂/nc-TiO₂/CH₃NH₃PbI_{3-x}Cl_x/P3HT/Au and FTO/c-TiO₂/nc-TiO₂/CH₃NH₃PbI_{3-x}Cl_x/spiro-OMeTAD/Au PSCs (Di Giacomo *et al.*, 2014) (c) J-V curves of series PSCs prepared by PbI₂ blade coating (Razza *et al.*, 2015)

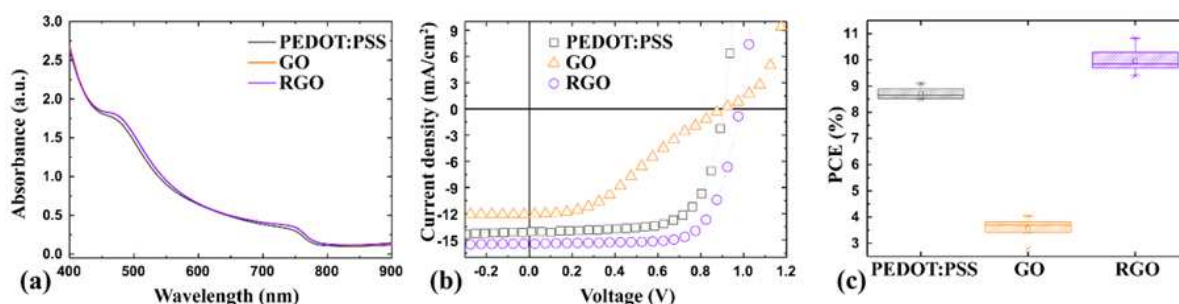


Fig. 19. (a) UV-vis absorption spectra (b) Current over voltage curves for PSC with various HTMs and (c) corresponding PCE statistics based on 20 devices (Yeo *et al.*, 2015)

Table 13. Average performance parameters of PSCs with HTM made of PEDOT: PSS, GO and RGO (Yeo *et al.*, 2015)

HTM	V _{OC} (V)	J _{SC} (mA/cm ²)	PCE (%)	FF (%)	R _s (ohm cm ²)
PEDOT: PSS	0.92	13.65	8.80(max. 9.14)	69.97	1.10
GO (graphene oxide)	0.89	10.70	3.58(max. 4.04)	37.61	3.15
RGO	0.95	14.81	9.95(max. 10.80)	71.13	0.92

Table 14. Effect of varying amount of ZnO nanoparticles in the PSC electrodes on its performance parameters (Lee *et al.*, 2014)

Electrode	V_{OC} (V)	J_{sc} (mA/cm ²)	η (%)	FF (%)
Reference (no modification)	1.022	14.78	11.23	0.73
10 wt.%ZnO	1.027	14.56	11.18	0.73
20 wt.%ZnO	1.020	14.86	10.92	0.71
30 wt.%ZnO	1.006	15.96	11.71	0.72
40 wt.%ZnO	0.993	15.24	10.90	0.71
50 wt.%ZnO	0.983	15.10	10.58	0.70

For example, Table 13 shows a comparison of PSC performance parameters between PSCs with HTM made of PEDOT: PSS, GO and RGO. Figures 19a-c show the performance curves of the three PSCs with varying HTM choices. This approach could motivate future researches into the design and development of HTMs and promise the improvement of PSC technology in terms of having lower cost with higher performance along the excellent stability (Yeo *et al.*, 2015).

Impact of PbI₂ Blade Coating as Air-Flow Assistance on PSC Performance

Blade coating can be performed in replacement of conventional spin coating to increase the deposition area. Blade coating can even reduce the use of material due to the peculiar compact structure of the PbI₂ obtained from blade-coating. To improve the efficiency, a long dipping time (30 min) into the CH₃NH₃I solution is required. By legitimate boost of the blade deposition and the air flow dynamics over the very large areas, most of the issues related with limited efficiency can be resolved. Figure 18c represents the current density over voltage characteristic curve of an 8 cm² module with 6.7% efficiency and large areas solar cells connected in series, prepared by PbI₂ blade coating deposition and 30 min of dipping in CH₃NH₃I solution. The V_{OC} of the complete module is the sum of the V_{OC} of each cell, indicating a good connection between the cells. The efficiency based on this PSC is reported to be up to 10.3% (Razza *et al.*, 2015).

Impact of ZnO Nanoparticles on TiO₂ Thin mp-Electrodes for PSC

By manipulating the mixing ratio of ZnO nanoparticles, the thin TiO₂ electrodes for two-step process sensitize for PSC can be modified. Table 14 illustrates the effect of varying amounts of ZnO nanoparticles in the electrodes on the performance parameters of PSC. The best efficiency result is obtained for the cell with electrodes containing 30 wt.% ZnO, as depicted by the performance curves of PSCs with non-modified electrodes and 30 wt% ZnO-modified electrodes shown in Fig. 20b and 20c. On the other hand, as shown in the two-step process in Fig. 20a, after the removal of the ZnO nanoparticles from the electrode structures, the increased current density is attributed to the facilitated conversion of molecular precursors to perovskite (Lee *et al.*, 2014).

To ensure that the performance results obtained are solely dependent on the modification of the mesoporous electrode, it is necessary to hold all other parameters such as film thickness and post processing steps constant. This method has proven itself as a viable alternative for better improvement of the efficiency in mesoporous and nanostructured solar cells (Lee *et al.*, 2014).

Impact of Low-Temperature Solution on High-Efficiency and High-Flexibility PSC Performance

The goal of thin film photovoltaics is to reduce the energy cost in solar panels compared to their silicon model. By using an electron collection layer, one of the highest efficiencies for the solution-processed PSC can be achieved. However, this electron collector layer needs to be sintered at 500°C. As shown in Table 15, the photovoltaic parameters of a low cost, solution-based disposition procedure nano-composites of TiO₂ nanoparticles and graphene as the electron collection layer in meso-superstruct PSC, is reported. Figure 21a and b, on the other hand, show the performance curves of the samples compared in Table 15 and the best-performing solar cells in bright and dark conditions respectively. The entire device can be fabricated with temperature less than 150°C due to the graphene nano-flakes that will provide superior charge collection in nano-composites. Based on Table 15, the graphene/metal oxide nano-composite has the potential as a low-cost solar cell. A relatively good absorbance for PSC can be achieved even with relatively easy solution-based process at low temperature using low-cost materials and on top of that the process does not rely on the use of elements in limited supply. Electron collection layers have a critical role in the most efficient thin film of PSC, as they facilitate selective charge collection. CdS, the most common commercial thin film of solar cell, has been in operation for this purpose also. They devote to parasitic absorption in the solar cell. It is necessary to mention that they can prevent leakage and shunting for the currents under reverse bias (Zhong *et al.*, 2015; You *et al.*, 2014).

Impact of Cesium-doped Methylammonium on Light Absorber Hybrid PSC Performance

This goal of Cesium doping is to improve the performance of inverted-type perovskite/fullerene planar heterojunction hybrid solar cells. Base on Table 16, high performance is achieved at 10% Cs doping in the MAPbI₃

perovskite structure, represented by enhancements in the morphology, device efficiency in light absorption and energy difference between the valance band. Because of the increment in the in short-circuit current density and open-circuit voltage) with light absorption in optimal device thickness, shown in Fig. 21c, this device efficiency

(with 10% Cs doped) is improved from 5.51 to 7.68%. Such approach to perovskite design offers the possibility to enhance the performance of conventional perovskite solar cells with n-type titania or alumina layers and to achieve even higher open-circuit voltages by employing tandem device structures (Choi *et al.*, 2014).

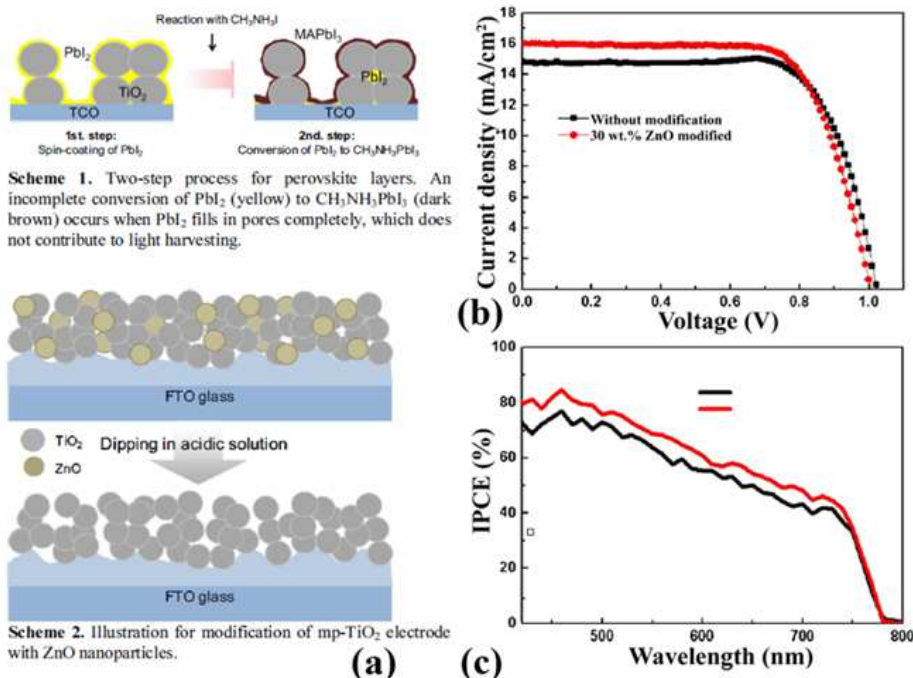


Fig. 20. (a) Schematic diagram of two-step sensitization process to fabricate ZnO-modified TiO_2 electrode for PSC (b) Current density over voltage curves and (c) IPCE curves of cells with unmodified electrode and 30 wt.% ZnO-modified electrode (Lee *et al.*, 2014)

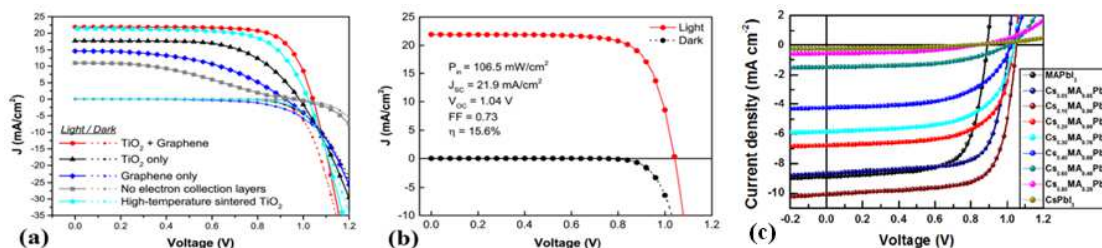


Fig. 21. (a) J-V characteristic curves of different electron collection layers under simulated AM 1.5, 100 mW/cm^2 solar irradiation (solid line) and in the dark (dotted line) (b) The best performing ($\eta = 15.6\%$) solar cell based on a graphene- TiO_2 nano-composites under simulated AM1.5, 106.5 mW/cm^2 solar irradiation (solid line) and in the dark (dotted line), which are processed at temperatures not exceeding 150°C (You *et al.*, 2014) (c) J-V characteristic curves of $Cs_xMA_{1-x}PbI_3$ perovskite devices with different Cs ratio (Choi *et al.*, 2014)

Table 15. Best-performing photovoltaics parameters based on disparate electron collection layer under simulated Am 1.5, 106.5 mW/cm^2 solar irradiation (You *et al.*, 2014)

Sample	V_{oc} (V)	J_{sc} (mA/cm^2)	PCE (%)	FF (%)	R_s (Ohm.cm^2)
No electron collection layer	0.95	10.8	3.7	37	79.1
TiO_2 only	1.00	17.7	10.0	61	10.1
Graphene only	0.90	14.6	5.9	48	20.3
$TiO_2 + graphene$	1.04	21.9	15.6	73	4.3
High temperature sintered TiO_2	1.00	21.4	14.1	70	5.9

Table 16. Photovoltaic characteristics of $Cs_xMA_{1-x}PbI_3$ PSC devices with different Cs ratio (Choi *et al.*, 2014)

Sample	V_{OC} (V)	J_{SC} (mA/cm ²)	PCE (%)	FF (%)
MAPbI ₃	0.89	8.89	5.51	0.70
Cs _{0.05} MA _{0.95} PbI ₃	1.01	8.69	6.29	0.72
Cs _{0.10} MA _{0.90} PbI ₃	1.05	10.10	7.68	0.73
Cs _{0.20} MA _{0.80} PbI ₃	1.04	6.76	4.58	0.65
Cs _{0.30} MA _{0.70} PbI ₃	1.04	5.85	3.78	0.62
Cs _{0.40} MA _{0.60} PbI ₃	1.03	4.26	2.50	0.57
Cs _{0.60} MA _{0.40} PbI ₃	1.01	1.50	0.79	0.52
Cs _{0.80} MA _{0.20} PbI ₃	0.84	0.58	0.22	0.46
CsPbI ₃	0.79	0.26	0.09	0.45

Table 17 Comparison of photovoltaic parameters with different sensitizers under AM1.5G simulation condition

Material	PCE (%)	FF	V_{OC} (V)	J_{SC} (mA/cm ²)	Remarks	References
Ass-PSSC (PANI + CH ₃ NH ₃ PbI ₃ + Li salt)	7.34±0.06	0.65±0.03	0.78±0.03	14.48±0.06	-	Xiao <i>et al.</i> (2014)
Ass-PSSC (PANI + CH ₃ NH ₃ PbI ₃)	5.13±0.04	0.54±0.02	0.74±0.03	12.84±0.05	-	Xiao <i>et al.</i> (2014)
Ass-PSSC (PANI only)	2.06±0.03	0.36±0.02	0.57±0.02	10.06±0.04	-	Xiao <i>et al.</i> (2014)
CH ₃ NH ₃ PbI ₃	12.7	0.68	0.98	19.1	-	Yamada <i>et al.</i> (2015)
CH ₃ NH ₃ PbI _{3-x} Cl _x + PVP	8.74	0.588	0.848	17.54	3.3% PVP	Ding <i>et al.</i> (2014)
CH ₃ NH ₃ PbI ₃	13.6	0.58±0.09	0.988±0.023	20.4±0.4	289±26 nm of CH ₃ NH ₃ PbI _{3-x} Cl _x	Della Gaspera <i>et al.</i> (2015)
Perovskite quantum-dots	6.2	0.617	0.629	15.99	-	Im <i>et al.</i> (2011)
N719	3.89	0.611	0.700	9.10	-	Im <i>et al.</i> (2011)
CH ₃ NH ₃ PbI _{3-x} Cl _x	15.4	0.67	1.07	21.5	Vapour deposited AM1.5 (101 mW/cm ²)	Liu <i>et al.</i> (2013)
	8.6	0.58	0.84	0.84	Solution processed AM1.5 (101 mW/cm ²)	
Submicrometer TiO ₂ NR sensitized with train ND	9.4	0.63	0.955	15.6	TiO ₂ -NR: L: 0.56 μm Diameter: 80 nm	Kim <i>et al.</i> (2013)

Summary of Various Impacts on PSC Performance

Besides the sensitizer itself, there are many other factors that influence the PSC efficiency. The sensitizer is only responsible in gaining high efficiency as it only converts the photons into electron-hole pairs. Certain sensitizers can carry out the conversion at certain wavelengths and different sensitizers can have very different recombination rates of electron-hole pairs. To complete the circuit however, the perovskite sensitizer will need to have the electrons and holes to be conducted in opposite directions and into the external circuit. The hole transport material, or HTM, is where the holes will be collected and the electron transport material, or ETM, is where the electrons will be collected. This collection process is crucial to prevent the recombination of electron-hole pairs within the sensitizer itself.

In order to optimize the efficiency through improvement of sensitizers, the focus is mainly on the structure of the sensitizer. The sensitizer is mostly made out of CH₃NH₃PbI₃ or mixed-halide CH₃NH₃PbI_{3-x}Cl_x material, fabricated in all-solid-state or combined with Li salt, or both. Moreover, the sensitizer can also be

fabricated alongside with poly-(vinylpyrrolidone) (PVP) to improve the efficiency. Table 17 summarizes the performance parameters of PSCs with several different sensitizer materials.

As one can observe in Table 15, HTM, which is to collect the holes generated by the sensitizer, have been shown to have a large impact on the PSC efficiency. Spiro-OMeTAD in PSCs is the most widely used HTM, while P3HT comes second. There are cost concerns when it comes to HTM materials, as spiro-OMeTAD is comparatively costly. Table 18 summarizes the performance parameters of PSCs with several different HTMs.

ETM is used to collect the electrons generated by the sensitizer. As ETM is generally made out of metal oxides, there are many different types of approaches in optimizing the ETM, including annealing and combining the ETM with other materials, or even embedding the sensitizer into the metal oxide itself. Some of the experiments have also shown that coating the sensitizers within the ETM will increase the efficiency and some have taken a different approach, that is to coat the sensitizer on top of a scaffolding TiO₂ layer. Table 19 summarizes the performance parameters of PSCs with several different ETMs.

Table 18 Comparison of photovoltaic parameters with different HTM under AM1.5 simulation condition

Material	PCE (%)	FF	V _{oc} (V)	J _{sc} (mA/cm ²)	Remark	References
No HTM	2.74	0.48	0.62	9.22	-	Nagarjuna <i>et al.</i> (2015)
P3HT	4.24	0.56	0.64	11.83	-	Nagarjuna <i>et al.</i> (2015)
D- π -A conjugated copolymer P	6.64	0.66	0.84	11.98	-	Nagarjuna <i>et al.</i> (2015)
P3HT / CH ₃ NH ₃ PbI _{3-x} Cl _x	9.3	0.58±0.05	0.93±0.06	12±3	-	Di Giacomo <i>et al.</i> (2014)
Spiro-OMeTAD / CH ₃ NH ₃ PbI _{3-x} Cl _x	8.6	0.60±0.05	0.84±0.03	12±2	-	Di Giacomo <i>et al.</i> (2014)
Cu2O (simulated result)	-	0.8397	1.276	22.75	Efficiency of 24.40%	Alharbi <i>et al.</i> (2014)
CuSCN	-	0.62	1.016	19.7	Efficiency of 12.40%	Alharbi <i>et al.</i> (2014)
NiO	-	0.75	0.936	14.9	Efficiency of 7.30%	Alharbi <i>et al.</i> (2014)
CuI]	-	0.60	0.550	17.8	Efficiency of 6.00%	Alharbi <i>et al.</i> (2014)

Table 19. Comparison of photovoltaic parameters with different ETM under AM1.5G simulation condition

Material	PCE/ η (%)	FF	V _{oc} (V)	J _{sc} (mA/cm ²)	Remarks	References
TiO ₂ + CH ₃ NH ₃ PbI ₃	9.7	0.62	0.888	17.6	-	Kim <i>et al.</i> (2012)
Compact-TiO ₂ amorphous	3.82	0.49	0.94	8.3	250°C; single layer	Yamamoto <i>et al.</i> (2014)
Compact-TiO ₂ anatase	1.47	0.33	0.87	5.2	450°C; single layer	Yamamoto <i>et al.</i> (2014)
	5.28	0.54	0.88	11.2	450°C; double layer	
Mesoscopic TiO ₂	12	0.673	0.886	19.97	-	Ramos <i>et al.</i> (2014)
Mesoporous TiO ₂ + CH ₃ NH ₃ PbI ₃	12.7	0.68	0.98	19.1	Embedded	Yamada <i>et al.</i> (2015)
TiO ₂ compact layer	12.1	0.75	1	17.35	-	Fakharuddin <i>et al.</i> (2015)
TiCl ₄ -nanorods	12.2	0.67	0.78	22.9	-	Fakharuddin <i>et al.</i> (2015)
TiO ₂ -nanococones	$\eta = 9.4$	0.63	0.955	15.6	TiO ₂ -nanococones at 1580 nm	Zhong <i>et al.</i> (2015);
	11.0	0.65	0.92	19.5	TiO ₂ -nanococones at 1400 nm	Kim <i>et al.</i> , (2013)
	10.4	0.583	0.94	19	TiO ₂ -nanococones at 1100 nm	
	$\eta = 7.3$	0.62	0.929	12.6	TiO ₂ -nanococones at 920 nm	
	10.3	0.552	1.02	18.4	TiO ₂ -nanococones at 700 nm	
	$\eta = 5.9$	0.61	0.865	11.2	TiO ₂ -nanococones at 560 nm	
TiO ₂ + Perovskite quantum dots	4.73	0.557	0.617	13.76	Annealing at 100°C	Im <i>et al.</i> (2011)
	6.2	0.617	0.629	15.99	TiO ₂ 3.6 nm thick	
ZnO-nanorods	11.13	0.56	0.991	20.08	1 μ m long 80 nm diameter	Son <i>et al.</i> (2014)
TiO ₂ \rightarrow Graphene	15.6	0.73	1.04	21.9	Low temperature AM1.5 (106.5 mW/cm ²)	Wang <i>et al.</i> (2014b)
ZnO-nanodots	14.4	69.6	1.01	20.5	Low temperature; 25 nm thick	Liu and Kelly (2014)
TiO ₂ with embedded CH ₃ NH ₃ PbI ₃	15	0.73	0.993	20.0	AM1.5G (96.4 mW/cm ²)	Burschka <i>et al.</i> (2013)
Mesoporous ZrO ₂	10.8	0.59	1.07	17.3	-	Bi <i>et al.</i> (2013)
TiO ₂ (TSD)	9.5	0.58	0.89	18.3	-	Bi <i>et al.</i> (2013)
ITO/PEIE/Y-TiO ₂ /Perovskite/Spiro-OMeTAD/Au	19.3	0.763	1.15	22.8	No reflective coating	Zhou <i>et al.</i> (2014)

Table 20. Comparison of photovoltaic parameters with multiple different parameters under AM1.5G simulation condition

Material	PCE (%)	FF	V _{oc} (V)	J _{sc} (mA/cm ²)	Remarks	References
CH ₃ NH ₃ PbI ₃	7.0	0.48	0.67	21.7	9th day; synthesized under ambient conditions	Sfyri <i>et al.</i> (2015)
Mesoporous TiO ₂ /CH ₃ NH ₃ PbI ₃ /Graphite/BM	0.25	0.317	0.845	0.6	Copper BM	Tripathi <i>et al.</i> (2015)
	0.9	0.224	0.83	4.85	FTO BM	
	1.11	0.445	0.702	3.56	Platinum BM	
b-MoO ₃ at transport top electrode	13.6	0.58±0.09	0.988±0.023	20.4±0.4	b-MoO ₃ at 5nm thick	Della Gaspera <i>et al.</i> (2015)
CH ₃ NH ₃ PbI _{3-x} Cl _x	14.08	0.7039	1.033	19.37	Annealed for 70 minutes	Song <i>et al.</i> (2015)
Rigid substrate	11.5	0.72	0.87	18.5	Glass/ITO substrate	You <i>et al.</i> (2014)
Flexible substrate	9.2	0.64	0.86	16.5	PET/ITO substrate (η drops after flexing)	You <i>et al.</i> (2014)
Flexible substrate	7	0.49	1.04	14.3	ETM = PCBM	Roldan-Carmona <i>et al.</i> , (2014)
					HTM = poly-TPD	
Flexible substrate after 50 bends	6.9	0.464	1.04	14.3	ETM = PCBM HTM = poly-TPD	Roldan-Carmona <i>et al.</i> , (2014)
200nm-mesoporous TiO ₂	16.46	0.76	1.105	19.58	FTO/BL-TiO ₂ /MP-TiO ₂ :MAPbI ₃ /UL-MAPbI ₃ /PTAA/Au	Jeon <i>et al.</i> (2014)

By changing some of the interface materials within the PSC device, the efficiency can change drastically. There are also some other experiments where the substrate has been changed from an ITO substrate/rigid

glass to a flexible PET/ITO substrate with a decrease in efficiency. When the flexible substrates are bent or rolled over for multiple times, the efficiency drops. Overall in terms of efficiency, there are a multitude of

variations in attempting higher efficiency, ranging from optimization of HTM and ETM, fabrication of sensitizer, crystal structure of ETM and how the sensitizer is embedded into the ETM itself. There are even hybrid materials where a combination of materials is used to fabricate the sensitizer.

Conclusion

Throughout the entire review paper, it can be noted that there are many different influences that will play a part in how perovskite can be manifested into commercial products without losing its properties. There are also many fabrication methods, ranging from commercial-friendly methods to highly sophisticated and costly methods. Some of the low-cost techniques have been tried and tested to fabricate PSC devices, such as spray pyrolysis technique (Razza *et al.*, 2015) and also spin coating of dye-sol paste (Ramos *et al.*, 2014).

With different tables of efficiency based on the variation of how the PSC device is made, it can be foreseen that a combination of said variations can be used to maximize the performance of future PSC. Flexible PSCs have also been fabricated, with a very good efficiency of 6.9% for a relatively new field (You *et al.*, 2014; Roldan-Carmona *et al.*, 2014). As the PSCs are made out of multiple layers of different materials, these layers, have shown its importance in the device.

We can see that there are certain optimizations done to the PSCs through different trials such as the data shown by Nagarjuna *et al.* (2015) where only the hole transport material layer is varied and it showed that the layer does indeed play a role in maximizing efficiency. In the sensitizer layer however, it has been said that the liquid electrolytes will pose a problem in the long run as it can potentially leak out or dried over time and thus Xiao *et al.* (2014) showed that with power conversion of 7.34%, an all-solid-state PSC can be done. The electron transport materials are mostly made out of metal oxides and is shown that the lattice structure of said metal oxide materials can also affect the efficiency drastically, as shown by Yamamoto *et al.* (2014). However, the fabrication of the ETM alone can incur a high cost onto the device, as sintering is required. Some of the experiments done had the sensitizer embedded into the ETM layer, resulting in an efficiency of 12.7% (Yamamoto *et al.*, 2014) and some have varied the number of layers of ETM to be fabricated and the resulting efficiency of double-layered ETM reached 5.28% (Yamamoto *et al.*, 2014).

Perovskite parade attractive and unusual physical properties which has persuaded the world to study it terms of the theoretical modeling and practical applications. Studies on perovskite were able to open the doors to the many revolutionary discoveries, which

allowed scientists to design devices with new concepts. Perovskite has a promising future due to low price, adaptability and thermal stability, which often depend on bulk and surface characteristics. The possibility of being coated on flexible or semi-transparent substrate, light weight thin-films are some advantages of PSC. Moreover, having high and rapidly improved efficiencies can also be characterized as advantages of this method. Even though there were many accomplishments on improvement of PSCs, but they are still on early stages of commercialization in compared to their more mature rivals. The main concerns with PSCs are still their steadiness and toxicity. By overcoming these two issues, PSCs can enter the commercial world and even mount among its rivals and become the main commercialized PSCs.

Acknowledgment

Authors would like to acknowledge Faculty of Engineering, Multimedia University for the support to conduct the review work. Author would also like to acknowledge Ministry of Higher Education (MOHE) to fund the Project under Fundamental Research Grant Scheme FRGS (MMUE150013).

Author's Contributions

All the Authors listed in this manuscript contributed significantly for the completion of the review article.

Alborz Ehtesham: Drafted the articles.

WongWei Wen: Wrote the critical review portion.

H.Y. Wong: Reviewed the article.

Mukter Zaman: Designed, planned and correspondent this article.

Ethics

Authors hereby confirming that there is no conflict of interest with this manuscript.

References

- Alharbi, F.H., M.I. Hossain and N. Tabet, 2014. Perovskite based solar cells: A milestone towards cheaper PV technology. Proceedings of the 3rd International Symposium on Environmental Friendly Energies and Applications, Nov. 19-21, IEEE Xplore Press, pp: 1-6.
DOI: 10.1109/EFEA.2014.7059955
- Bi, D., S.J. Moon, L. Haggman, G. Boschloo and L. Yang *et al.*, 2013. Using a two-step deposition technique to prepare perovskite (CH₃NH₃PbI₃) for thin film solar cells based on ZrO₂ and TiO₂ mesostructures. RSC Adv., 3: 18762-18766.
DOI: 10.1039/C3RA43228A

- Boix, P.P., K. Nonomura, N. Mathews and S.G. Mhaisalkar, 2014. Current progress and future perspectives for organic/inorganic perovskite solar cells. *Mater. Today*, 17: 16-23.
DOI: 10.1016/j.mattod.2013.12.002
- Bradley, D., 2015. Perovskite promise for solar energy. *Mater. Today*, 18: 124-125.
DOI: 10.1039/C4EE03322A
- Burschka, J., N. Pellet, S.J. Moon, R. Humphry-Baker and P. Gao *et al.*, 2013. Sequential deposition as a route to high-performance perovskite-sensitized solar cells. *Nature*, 499: 316-319.
DOI: 10.1038/nature12340
- Choi, H., J. Jeong, H.B. Kim, S. Kim and B. Walker *et al.*, 2014. Cesium-doped methylammonium lead iodide perovskite light absorber for hybrid solar cells. *Nano Energy*, 7: 80-85.
DOI: 10.1016/j.nanoen.2014.04.017
- Cimaroli, A. and Y. Yanfa, 2014. Characterization of ion-assisted, coevaporated $\text{CH}_3\text{NH}_3\text{PbI}_3$ thin films. Proceedings of the IEEE 40th Photovoltaic Specialist Conference, Jun. 8-13, IEEE Xplore Press, pp: 1522-1524.
DOI: 10.1109/PVSC.2014.6925205
- Della Gaspera, E., Y. Peng, Q. Hou, L. Spiccia and U. Bach *et al.*, 2015. Ultra-thin high efficiency semitransparent perovskite solar cells. *Nano Energy*, 13: 249-257. DOI: 10.1016/j.nanoen.2015.02.028
- Di Giacomo, F., S. Razza, F. Matteocci, A. D'Epifanio and S. Licoccia *et al.*, 2014. High efficiency $\text{CH}_3\text{NH}_3\text{PbI}_{(3-x)}\text{Cl}_x$ perovskite solar cells with poly(3-hexylthiophene) hole transport layer. *J. Power Sources*, 251: 152-156.
DOI: 10.1016/j.jpowsour.2013.11.053
- Ding, Y., X. Yao, X. Zhang, C. Wei and Y. Zhao, 2014. Surfactant enhanced surface coverage of $\text{CH}_3\text{NH}_3\text{PbI}_{3-x}\text{Cl}_x$ perovskite for highly efficient mesoscopic solar cells. *J. Power Sources*, 272: 351-355. DOI: 10.1016/j.jpowsour.2014.08.095
- Dkhissi, Y., F. Huang, S. Rubanov, M. Xiao and U. Bach *et al.*, 2015. Low temperature processing of flexible planar perovskite solar cells with efficiency over 10%. *J. Power Sources*, 278: 325-331.
DOI: 10.1016/j.jpowsour.2014.12.104
- Fakharuddin, A., F. Di Giacomo, I. Ahmed, Q. Wali and T.M. Brown *et al.*, 2015. Role of morphology and crystallinity of nanorod and planar electron transport layers on the performance and long term durability of perovskite solar cells. *J. Power Sources*, 283: 61-67.
DOI: 10.1016/j.jpowsour.2015.02.084
- Ghiasi, M. and A. Malekzadeh, 2014. Solar photocatalytic degradation of methyl orange over $\text{La}_{0.7}\text{Sr}_{0.3}\text{MnO}_3$ nano-perovskite. *Separat. Purificat. Technol.*, 134: 12-19.
DOI: 10.1016/j.seppur.2014.07.022
- Green, M.A., A. Ho-Baillie and H.J. Snaith, 2014. The emergence of perovskite solar cells. *Nat. Photon.*, 8: 506-514. DOI: 10.1038/nphoton.2014.134
- Huang, Y., Y. Wei, S. Cheng, L. Fan and Y. Li *et al.*, 2010. Photocatalytic property of nitrogen-doped layered perovskite $\text{K}_2\text{La}_2\text{Ti}_3\text{O}_{10}$. *Solar Energy Mater. Solar Cells*, 94: 761-766.
DOI: 10.1016/j.solmat.2009.12.020
- Im, J.H., C.R. Lee, J.W. Lee, S.W. Park and N.G. Park, 2011. 6.5% efficient perovskite quantum-dot-sensitized solar cell. *Nanoscale*, 3: 4088-4093.
DOI: 10.1039/C1NR10867K
- Jeon, N.J., J.H. Noh, Y.C. Kim, W.S. Yang and S. Ryu *et al.*, 2014. Solvent engineering for high-performance inorganic-organic hybrid perovskite solar cells. *Nat. Mater.*, 13: 897-903.
DOI: 10.1038/nmat4014
- Jianping, D., L. Jing, W. Minqiang and S. Xiaohui, 2014. The influence of blocking layer on the photovoltaic performance of organometal halide perovskite solar cell. Proceedings of the IEEE 14th International Conference on Nanotechnology, Aug. 18-21, IEEE Xplore Press, pp: 789-793.
DOI: 10.1109/NANO.2014.6968104
- Kim, B.S., T.M. Kim, M.S. Choi, H.S. Shim and J.J. Kim, 2015. Fully vacuum-processed perovskite solar cells with high open circuit voltage using MoO_3/NPB as hole extraction layers. *Organic Electron.*, 17: 102-106.
DOI: 10.1016/j.orgel.2014.12.002
- Kim, H.S., C.R. Lee, J.H. Im, K.B. Lee and T. Moehl *et al.*, 2012. Lead iodide perovskite sensitized all-solid-state submicron thin film mesoscopic solar cell with efficiency exceeding 9%. *Scientific Rep.*, 2: 591-591.
DOI: 10.1038/srep00591
- Kim, H.S., J.W. Lee, N. Yantara, P.P. Boix and S.A. Kulkarni *et al.*, 2013. High efficiency solid-state sensitized solar cell-based on submicrometer rutile TiO_2 nanorod and $\text{CH}_3\text{NH}_3\text{PbI}_3$ perovskite sensitizer. *Nano Lett.*, 13: 2412-2417.
DOI: 10.1021/nl400286w
- Lee, Y.H., M. Stefiik, L.P. Heiniger, P. Gao and S. Il Seok *et al.*, 2014. Power from the sun: Perovskite solar cells. Proceedings of the IEEE 40th Photovoltaic Specialist Conference, Jun. 8-13, IEEE Xplore Press, pp: 0943-0948. DOI: 10.1109/PVSC.2014.6925068
- Li, X., X. Wang, W. Zhang, Y. Wu and F. Gao *et al.*, 2015. The effect of external electric field on the performance of perovskite solar cells. *Organic Electron.*, 18: 107-112. DOI: 10.1016/j.orgel.2015.01.024
- Liu, C., Z. Qiu, W. Meng, J. Chen and J. Qi *et al.*, 2015. Effects of interfacial characteristics on photovoltaic performance in $\text{CH}_3\text{NH}_3\text{PbBr}_3$ -based bulk perovskite solar cells with core/shell nanoarray as electron transporter. *Nano Energy*, 12: 59-68.
DOI: 10.1016/j.nanoen.2014.12.004

- Liu, D. and T.L. Kelly, 2014. Perovskite solar cells with a planar heterojunction structure prepared using room-temperature solution processing techniques. *Nat. Photon.*, 8: 133-138. DOI: 10.1038/nphoton.2013.342
- Liu, M., M.B. Johnston and H.J. Snaith, 2013. Efficient planar heterojunction perovskite solar cells by vapour deposition. *Nature*, 501: 395-398. DOI: 10.1038/nature12509
- Minemoto, T. and M. Murata, 2014. Impact of work function of back contact of perovskite solar cells without hole transport material analyzed by device simulation. *Curr. Applied Phys.*, 14: 1428-1433. DOI: 10.1016/j.cap.2014.08.002
- Minemoto, T. and M. Murata, 2015. Theoretical analysis on effect of band offsets in perovskite solar cells. *Solar Energy Mater. Solar Cells*, 133: 8-14. DOI: 10.1016/j.solmat.2014.10.036
- Nagarajuna, P., K. Narayanaswamy, T. Swetha, G.H. Rao and S.P. Singh *et al.*, 2015. CH₃NH₃PbI₃ Perovskite Sensitized Solar Cells Using a D-A Copolymer as Hole Transport Material. *Electrochim. Acta*, 151: 21-26. DOI: 10.1016/j.electacta.2014.11.003
- Ogomi, Y., A. Morita, S. Tsukamoto, T. Saitho and N. Fujikawa *et al.*, 2014. All-solid Sn/Pb halide perovskite sensitized solar cells. *Proceedings of the IEEE 40th Photovoltaic Specialist Conference*, Jul. 8-13, IEEE Xplore Press, pp: 0151-0155. DOI: 10.1109/PVSC.2014.6925439
- Peplow, M., 2014. The Perovskite revolution [News]. *IEEE Spectrum*, 51: 16-17, 2014. DOI: 10.1109/MSPEC.2014.6840788
- Ramos, F.J., D. Cortes, A. Aguirre, F.J. Castano and S. Ahmad, 2014. Fabrication and encapsulation of perovskites sensitized solid state solar cells. *Proceedings of the IEEE 40th Photovoltaic Specialist Conference*, Jun. 8-13, IEEE Xplore Press, pp: 2584-2587. DOI: 10.1109/PVSC.2014.6925459
- Razza, S., F. Di Giacomo, F. Matteocci, L. Cinà and A.L. Palma *et al.*, 2015. Perovskite solar cells and large area modules (100 cm²) based on an air flow-assisted PbI₂ blade coating deposition process. *J. Power Sources*, 277: 286-291. DOI: 10.1016/j.jpowsour.2014.12.008
- Roldan-Carmona, C., O. Malinkiewicz, A. Soriano, G. Minguez Espallargas and A. Garcia *et al.*, 2014. Flexible high efficiency perovskite solar cells. *Energy and Environ. Sci.*, 7: 994-997. DOI: 10.1039/C3EE43619E
- Senthilarasu, S., E.F. Fernández, F. Almonacid and T.K. Mallick, 2015. Effects of spectral coupling on perovskite solar cells under diverse climatic conditions. *Solar Energy Mater. Solar Cells*, 133: 92-98. DOI: 10.1016/j.solmat.2014.10.037
- Sfyri, G., C.V. Kumar, D. Raptis, V. Dracopoulos and P. Lianos, 2015. Study of perovskite solar cells synthesized under ambient conditions and of the performance of small cell modules. *Solar Energy Mater. Solar Cells*, 134: 60-63. DOI: 10.1016/j.solmat.2014.11.034
- Sheikh, A.D., A. Bera, M.A. Haque, R.B. Rakhi and S.D. Gobbo *et al.*, 2015. Atmospheric effects on the photovoltaic performance of hybrid perovskite solar cells. *Solar Energy Mater. Solar Cells*, 137: 6-14. DOI: 10.1016/j.solmat.2015.01.023
- Son, D.Y., J.H. Im, H.S. Kim and N.G. Park, 2014. 11% efficient perovskite solar cell based on ZnO nanorods: An effective charge collection system. *J. Phys. Chem. C*, 118: 16567-16573. DOI: 10.1021/jp412407j
- Song, T.B., Q. Chen, H. Zhou, S. Luo and Y. Yang *et al.*, 2015. Unraveling film transformations and device performance of planar perovskite solar cells. *Nano Energy*, 12: 494-500. DOI: 10.1016/j.nanoen.2015.01.025
- Tathavadekar, M.C., S.A. Agarkar, O.S. Game, U.P. Bansode and S.A. Kulkarni *et al.*, 2015. Enhancing efficiency of perovskite solar cell via surface microstructuring: Superior grain growth and light harvesting effect. *Solar Energy*, 112: 12-19. DOI: 10.1016/j.solener.2014.11.016
- Tress, W., N. Marinova, O. Inganas, M.K. Nazeeruddin and S.M. Zakeeruddin *et al.*, 2014. The role of the hole-transport layer in perovskite solar cells-reducing recombination and increasing absorption. *Proceedings of the IEEE 40th Photovoltaic Specialist Conference*, Jun. 8-13, IEEE Xplore Press, pp: 1563-1566. DOI: 10.1109/PVSC.2014.6925216
- Tripathi, B., P. Bhatt, P. Chandra Kanth, P. Yadav and B. Desai *et al.*, 2015. Temperature induced structural, electrical and optical changes in solution processed perovskite material: Application in photovoltaics. *Solar Energy Mater. Solar Cells*, 132: 615-622. DOI: 10.1016/j.solmat.2014.10.017
- Wang, X., Y. Fang, L. He, Q. Wang and T. Wu, 2014a. Influence of compact TiO₂ layer on the photovoltaic characteristics of the organometal halide perovskite-based solar cells. *Mater. Sci. Semiconductor Process.*, 27: 569-576. DOI: 10.1016/j.mssp.2014.07.039
- Wang, J.T.W. J.M. Ball, E.M. Barea, A. Abate and J.A. Alexander-Webber *et al.*, 2014b. Low-temperature processed electron collection layers of graphene/TiO₂ nanocomposites in thin film perovskite solar cells. *Nano Lett.*, 14: 724-730. DOI: 10.1021/nl403997a
- Wang, K., C. Liu, P. Du, L. Chen and J. Zhu *et al.*, 2015. Efficiencies of perovskite hybrid solar cells influenced by film thickness and morphology of CH₃NH₃PbI_{3-x}Cl_x layer. *Organic Electron.*, 21: 19-26. DOI: 10.1016/j.orgel.2015.02.023

- Wasa, K., I. Kanno, H. Kotera, N. Yamauchi and T. Matsushima, 2016. Thin films of PZT-based ternary perovskite compounds for MEMS. Proceedings of the IEEE Ultrasonics Symposium, Nov. 2-5, IEEE Xplore Press, pp: 213-216.
DOI: 10.1109/ULTSYM.2008.0052
- Woojun, Y., J.E. Boercker, M.P. Lumb, J.G. Tischler and P.P. Jenkins *et al.*, 2014. Vapor deposition of organic-inorganic hybrid perovskite thin-films for photovoltaic applications. Proceedings of the IEEE 40th Photovoltaic Specialist Conference, Jun. 8-13, IEEE Xplore Press, pp: 1577-1580.
DOI: 10.1109/PVSC.2014.6925219
- Xiao, Y., G. Han, Y. Chang, H. Zhou and M. Li *et al.*, 2014. An all-solid-state perovskite-sensitized solar cell based on the dual function polyaniline as the sensitizer and p-type hole-transporting material. J. Power Sources, 267: 1-8.
DOI: 10.1016/j.jpowsour.2014.05.053
- Xin, F., P. Xiaoli, Z. Shu and X. Yong, 2014. Fabrication of planar heterojunction perovskite solar cells. Proceedings of the International Symposium on Next-Generation Electronics, May 7-10, IEEE Xplore Press, pp: 1-2.
DOI: 10.1109/ISNE.2014.6839359
- Yamada, Y., T. Nakamura, M. Endo, A. Wakamiya and Y. Kanemitsu, 2015. Photoelectronic responses in solution-processed perovskite CH₃ NH₃PbI₃ solar cells studied by photoluminescence and photoabsorption spectroscopy. IEEE J. Photovolta., 5: 401-405. DOI: 10.1109/JPHOTOV.2014.2364115
- Yamamoto, K., Z. Ying, T. Kuwabara, K. Takahashi and M. Endo *et al.*, 2014. Low temperature TiO_x compact layer by chemical bath deposition method for vapor deposited perovskite solar cells. Proceedings of the IEEE 40th Photovoltaic Specialist Conference, Jun 8-13, IEEE Xplore Press, pp: 1573-1576. DOI: 10.1109/PVSC.2014.6925218
- Yeo, J.S., R. Kang, S. Lee, Y.J. Jeon and N. Myoung *et al.*, 2015. Highly efficient and stable planar perovskite solar cells with reduced graphene oxide nanosheets as electrode interlayer. Nano Energy, 12: 96-104.
DOI: 10.1016/j.nanoen.2014.12.022
- You, J., Z. Hong, Y. Yang, Q. Chen and M. Cai *et al.*, 2014. Low-temperature solution-processed perovskite solar cells with high efficiency and flexibility. ACS Nano, 8: 1674-1680.
DOI: 10.1021/nn406020d
- Zhang, Y., W. Liu, F. Tan and Y. Gu, 2015. The essential role of the poly(3-hexylthiophene) hole transport layer in perovskite solar cells. J. Power Sources, 274: 1224-1230.
DOI: 10.1016/j.jpowsour.2014.10.145
- Zhong, D., B. Cai, X. Wang, Z. Yang and Y. Xing *et al.*, 2015. Synthesis of oriented TiO₂ nanocones with fast charge transfer for perovskite solar cells. Nano Energy, 11: 409-418.
DOI: 10.1016/j.nanoen.2014.11.014
- Zhou, H., Q. Chen, G. Li, S. Luo and T.B. Song *et al.*, 2014. Interface engineering of highly efficient perovskite solar cells. Science, 345: 542-546.
DOI: 10.1126/science.1254050